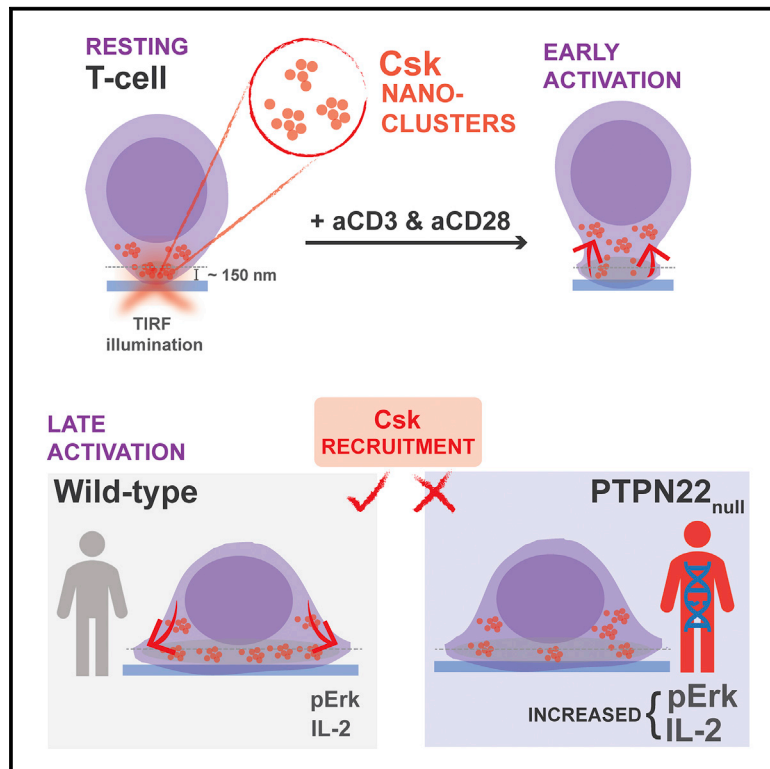


Multi-color Molecular Visualization of Signaling Proteins Reveals How C-Terminal Src Kinase Nanoclusters Regulate T Cell Receptor Activation

Graphical Abstract



Authors

Sabrina Simoncelli, Juliette Griffié, David J. Williamson, ..., Rose Zamoyska, Andrew P. Cope, Dylan M. Owen

Correspondence

s.simoncelli@ucl.ac.uk (S.S.),
d.owen@bham.ac.uk (D.M.O.)

In Brief

Simoncelli et al. use DNA-PAINT, a super-resolution microscopy technique, to resolve the nanoscale organization of three proteins implicated with T cell signaling downregulation. Quantitative analysis reveals the inhibitory protein Csk exists in nanoscale clusters close to the membrane that leave during early activation and later return to restore its function.

Highlights

- DNA-based super-resolution enables imaging of individual proteins in dense clusters
- Csk forms nanoclusters that change their localization during T cell activation
- Csk nanoclusters do not coalesce with PAG or TRAF3
- Csk recruitment during late T cell activation is impaired in the absence of PTPN22



Resource

Multi-color Molecular Visualization of Signaling Proteins Reveals How C-Terminal Src Kinase Nanoclusters Regulate T Cell Receptor Activation

Sabrina Simoncelli,^{1,2,*} Juliette Griffié,^{1,3} David J. Williamson,¹ Jack Bibby,^{4,5} Cara Bray,⁶ Rose Zamoyska,⁶ Andrew P. Cope,⁴ and Dylan M. Owen^{1,7,8,*}

¹Department of Physics and Randall Centre for Cell and Molecular Biophysics, Faculty of Life Sciences and Medicine, King's College London, London SE1 1UL, UK

²London Centre for Nanotechnology and Department of Chemistry, University College London, London WC1H 0AH, UK

³Laboratory for Experimental Biophysics, Institute of Physics, École Polytechnique Fédérale de Lausanne (EPFL), 1015 Lausanne, Switzerland

⁴Centre for Rheumatic Diseases, School of Immunology and Microbial Sciences, Faculty of Life Sciences and Medicine, King's College London, London SE1 1UL, UK

⁵Complement and Inflammation Research Section (CIRS), National Heart, Lung, and Blood Institute, National Institutes of Health, Bethesda, MD 20892, USA

⁶Institute of Immunology and Infection Research, Centre for Immunity, Infection and Evolution, University of Edinburgh, Edinburgh EH9 3FL, UK

⁷Institute of Immunology and Immunotherapy, Department of Mathematics and Centre of Membrane Proteins and Receptors, University of Birmingham, Birmingham, UK

⁸Lead Contact

*Correspondence: s.simoncelli@ucl.ac.uk (S.S.), d.owen@bham.ac.uk (D.M.O.)

<https://doi.org/10.1016/j.celrep.2020.108523>

SUMMARY

Elucidating the mechanisms that controlled T cell activation requires visualization of the spatial organization of multiple proteins on the submicron scale. Here, we use stoichiometrically accurate, multiplexed, single-molecule super-resolution microscopy (DNA-PAINT) to image the nanoscale spatial architecture of the primary inhibitor of the T cell signaling pathway, Csk, and two binding partners implicated in its membrane association, PAG and TRAF3. Combined with a newly developed co-clustering analysis framework, we find that Csk forms nanoscale clusters proximal to the plasma membrane that are lost post-stimulation and are re-recruited at later time points. Unexpectedly, these clusters do not co-localize with PAG at the membrane but instead provide a ready pool of monomers to downregulate signaling. By generating CRISPR-Cas9 knockout T cells, our data also identify that a major risk factor for autoimmune diseases, the protein tyrosine phosphatase non-receptor type 22 (PTPN22) locus, is essential for Csk nanocluster re-recruitment and for maintenance of the synaptic PAG population.

INTRODUCTION

Protein clustering at the nanoscale appears to be integral to determining the fate of T cell receptor (TCR) early activation (Sherman et al., 2013). Because clusters are small, they have been extensively studied by single-molecule localization microscopy (SMLM), such as PALM (photoactivated localization microscopy) (Betzig et al., 2006) and STORM (stochastic optical reconstruction microscopy) (Rust et al., 2006). Previous studies have shown that following TCR engagement, the number and/or density of clusters of cell surface receptors (TCRs [Lillemeier et al., 2010] and integrins [van Zanten et al., 2009]), activating kinases (e.g., Lck [Rossey et al., 2013] and ZAP-70 [Katz et al., 2017]), and adaptor proteins (e.g., LAT [Lillemeier et al., 2010; Williamson et al., 2011]) generally increases. However, because of the difficulties in quantifying the exact protein copy number in

SMLM data, different imaging modalities identify diverse protein cluster configurations that range from dimers/trimers to larger islands and aggregates, opening questions about data interpretation (Feher et al., 2019).

Therefore, dissecting the role of nanoscale clustering in TCR signaling requires super-resolution imaging techniques that allow accurate quantification of the protein copy number (Feher et al., 2019; Rossoboth et al., 2018). SMLM is based on temporally separating the fluorescence of single molecules such that only a subset of fluorophores are detected and localized with nanometer-scale precision by fitting point spread functions in each camera frame. Temporal isolation in PALM or STORM is achieved by photoactivation or by stochastically switching fluorophores between a dark and a fluorescent state, respectively. This causes some fluorophores to be detected multiple times over acquisition with nearly identical coordinates. Although different efforts have



been made to account for these multiple observations, they require either careful calibration and knowledge of the complex photophysical properties of the fluorophores (Lee et al., 2012; Rollins et al., 2015; Nieuwenhuizen et al., 2015) or multiple, time-consuming experiments varying the label concentration (Baumgart et al., 2016). In the case of dSTORM (direct-STORM), antibodies might have multiple fluorophores attached to them, leading to overcounting or multiple detection issues. In this regard, DNA-PAINT (a variation of point accumulation for imaging in nanoscale topography) (Schnitzbauer et al., 2017), which is a robust SMLM technique that relies on the binding kinetics between two single-stranded DNAs (ssDNAs: imager and docking strands), has recently shown impressive advances in quantifying, from single-molecule localization data, individual molecular targets on synthetic samples that simulate bio-molecular nanoclusters (qPAINT) (Dai et al., 2016). This is possible because unlike other SMLM methods, DNA-PAINT is independent of the dye's complex photophysics, making it possible to easily correlate the frequency of single-molecule events with the underlying number of labeled molecular targets (Jungmann et al., 2016). Furthermore, DNA-PAINT enables multi-color imaging by sequential washout and exchange of imager strands, which is not possible with more traditional SMLM (Jungmann et al., 2014). Because of the comparative advantages of DNA-PAINT over other SMLM techniques, we used this imaging approach to dissect the functional implications of C-terminal Src kinase (Csk) nano-clustering and its spatial organization.

Csk is the most potent inhibitor of Lck, the primary tyrosine kinase to propagate signaling in T cells (Bergman et al., 1992). Lck adopts an active conformation through the autophosphorylation of Tyr³⁹⁴, whereas phosphorylation of its Tyr⁵⁰⁵ residue by Csk promotes its closed, inactive conformation (Dobenecker et al., 2005). Csk exerts a tonic inhibition of membrane-associated Lck in resting T cells, which appears to set the threshold for TCR activation (Nada et al., 1993; Schmedt et al., 1998). Therefore, for efficient TCR signaling to occur, Csk must translocate away from the membrane-proximal signaling zone to the cytosol (Torgersen et al., 2001). However, the Lck activation phase only last for minutes before Csk is re-recruited to the membrane to downmodulate TCR signaling (Torgersen et al., 2001). Because Csk is constitutively active in T cells, its relative spatial localization is believed to be critical for regulating TCR signaling. Being a cytosolic protein that lacks any anchor for membrane association, Csk relies on its interaction with transmembrane proteins to achieve this spatial translocation (Kawabuchi et al., 2000). Several reports have shown that PAG (phosphoprotein associated with glycolipid-enriched microdomains) phosphorylation at Tyr³¹⁷ controls Csk association and dissociation from lipid rafts at the plasma membrane (Hrdinka and Horejsi, 2014). Conversely, TRAF3 (tumor necrosis factor receptor-associated factor) has been suggested to act as a chaperone that promotes Csk translocation to the cytoplasm following TCR engagement (Wallis et al., 2017). Although numerous studies underline the importance of Csk translocation from the membrane to the cytosol for TCR activation, the underlying mechanism of Csk regulatory duty is unclear.

Here, we couple DNA-PAINT with state-of-the-art Bayesian-based cluster analysis to convert SMLM data to stoichiometri-

cally accurate multi-channel nanoscale protein distribution maps to quantitatively characterize the nanoscale architecture of Csk, PAG, and TRAF3 in resting T cells and the T cell immunological synapse. Our data provide new evidence describing, at the single-molecule level, how Csk regulates Lck activity, addressing precisely how PAG and TRAF3 are involved. We find that the dynamic nanoscale organization of Csk is indeed a key regulatory element in TCR-induced signal activation and termination and that it does not involve the formation of 3-component Csk, PAG, and TRAF3 complexes. We also show that the absence of the most relevant binding partner for Csk, protein tyrosine phosphatase non-receptor type 22 (PTPN22) (Stanford and Bottini, 2014), aberrates Csk nanoarchitecture with consequences for downstream signaling. Csk and PTPN22 interaction is especially interesting, because it is disrupted in more than 10% of the white population, leading to several autoimmune diseases in humans (Siminovitch, 2004; Stanford and Bottini, 2014). Our data show that in the absence of PTPN22, there is a marked failure to recruit back Csk during late synapses. This work therefore provides a new technology platform for the precise dissection of signaling pathways and new insights into the interplay of kinases and phosphatases in balancing T cell activation, with implications for understanding immune responses and autoimmune disease.

RESULTS

Super-resolution Imaging of Csk, PAG, and TRAF3 Nanoarchitecture in T Cells Using DNA-PAINT

To characterize the processes whereby Csk downregulates TCR signaling, we examined the nanoscale organization of Csk, PAG, and TRAF3 at different time points in wild-type (WT) and PTPN22 knockout (KO) Jurkat T cells proximal to the plasma membrane using DNA-PAINT under total internal reflection (TIR) excitation (Figure 1; Figure S1). DNA-PAINT (Schnitzbauer et al., 2017) employs the transient binding of short fluorescently labeled oligonucleotides (imager strands) to complementary ssDNA targets (docking strands) chemically coupled to antibodies (Figure 1A; Figure S2A). While bound, the imager strand can be imaged and localized with nanometer precision. Through sequential imaging of different imager strand sequences targeting different docking strands and their antibodies, DNA-PAINT overcomes the limitations of other SMLM techniques for multi-color imaging. To label the proteins for DNA-PAINT imaging, we used monoclonal antibodies conjugated at a ~1-to-1 ratio to unique ssDNA docking strand sequences. We sequentially imaged with the complementary imager strands, each fluorescently labeled with ATTO655, and reconstructed the single-molecule localization maps of each protein (Figures 1C–1E, top; Figure S1, middle and bottom).

We developed a sophisticated cluster analysis pipeline that allows conversion of DNA-PAINT single-molecule localizations maps (Figures 1C–1E, middle) into antibody-labeled protein copy number maps (Figures 1C–1E, bottom). In DNA-PAINT, a DNA-coupled antibody is localized a predictable number of times, rendering a cluster of localizations around the true position of the protein (Figure 1B), whereas non-specific binding events are detected as non-clustered localizations. Using a

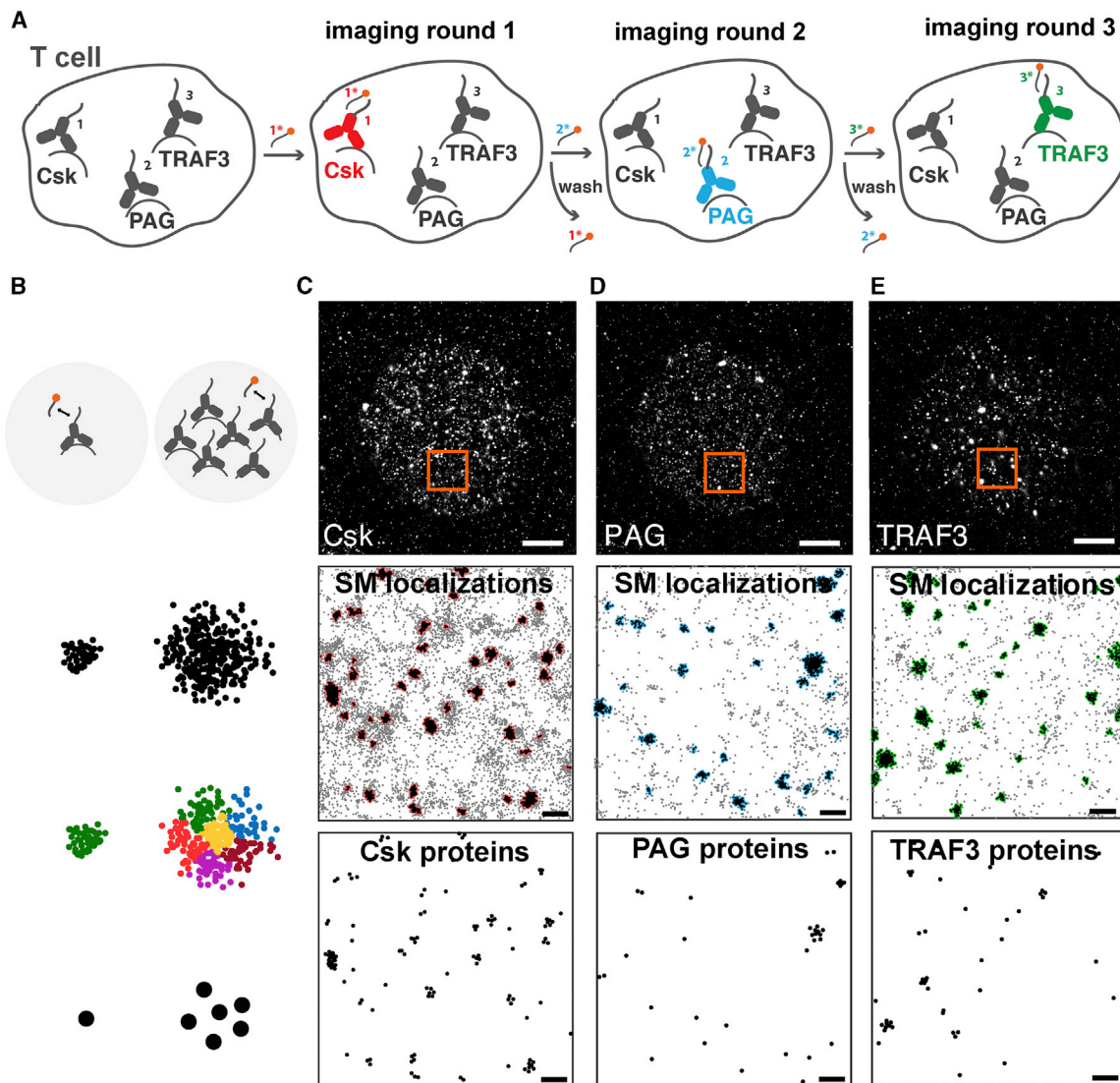


Figure 1. Exchange-DNA-PAINT Imaging of Csk, PAG, and TRAF3 in WT Jurkat T Cells

(A) Schematic representation of Exchange-DNA-PAINT imaging.

(B) In DNA-PAINT, the number of sites can be calculated using the binding kinetic information between fluorescently labeled imager strands and their complementary docking strands attached to the target antibodies. Using the k-means function, it is then possible to recover the most likely distribution of sites from the single-molecule localizations distribution.

(C–E) DNA-PAINT single-molecule (SM) localization maps (top) of WT Jurkat T cells supported on glass coated with poly-L-lysine (PLL) before they were fixed, permeabilized, and stained with mouse anti-Csk, anti-PAG, and anti-TRAF3 antibodies, each carrying a unique 11 nt ssDNA (docking strand). Images were acquired by sequential imaging with each of the complementary DNA strands labeled with ATTO655 (imager strand) under total internal reflection illumination. Single-molecule localization distributions (points) were analyzed with a cluster analysis algorithm based on Ripley's K function, Bayesian statistics, and topographical prominence to identify cluster points (red, blue, or green outlined) in $4 \mu\text{m}^2$ region maps (center, boxed region). Cluster points were converted into the most likely descriptor of Csk (C), PAG (D), and TRAF3 (E) protein maps (bottom). Scale bars represent $2 \mu\text{m}$ (top) and 200nm (center and bottom).

See also [Figures S1](#) and [S2](#).

custom-designed nanoscale DNA-origami platform, we calibrated, for our experimental imaging condition, the expected number of localizations per molecular target to be 52 ± 6 per 10,000 frames and showed that the localization-labeled target relationship is linear over 20 molecular targets, with a counting error lower than 10% ([Figure S2C](#)). We found that this value agrees well with the intrinsic calibration presented in [Figures](#)

[S2F–S2H](#) for Csk, PAG, and TRAF3 single-molecule localization data in T cells. As such, we used it to estimate the number of labeled proteins from DNA-PAINT data. Alternatively, and as a general approach useful when a higher number of molecular targets per cluster are expected, the distribution of dark times within each cluster can also be used to effectively determine the underlying number of labeled proteins, as originally

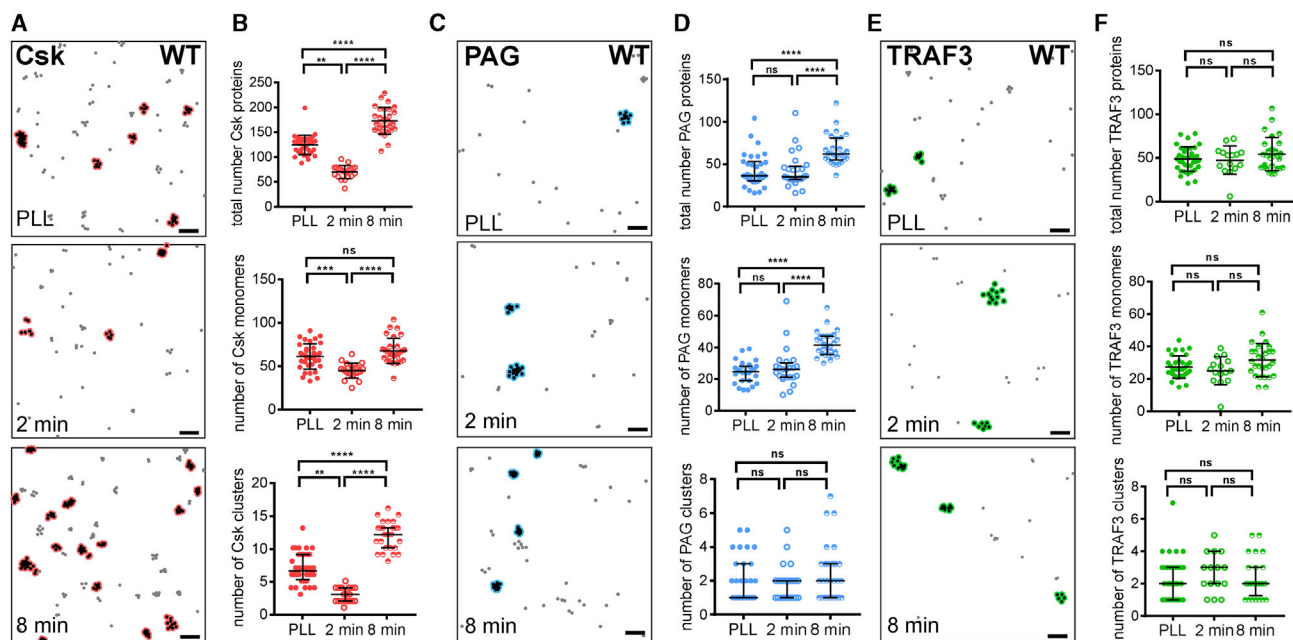


Figure 2. Csk and PAG Are Recruited Back En Masse to the Membrane during Late Synapses

Csk (A), PAG (C), or TRAF3 (E) protein maps reconstructed from the localization maps of WT Jurkat T cells supported on glass coated with PLL (top) or anti-CD3/anti-CD28 for either 2 min (center) or 8 min (bottom). For each condition, protein map distributions were analyzed using a Bayesian-based cluster analysis to identify cluster points (red, blue, or green outlined) and extract their properties. Selected descriptors from the cluster analysis of Csk (B), PAG (D), and TRAF3 (F) protein maps representing total number of proteins (top), number of non-clustered proteins (center), and number of clusters (bottom) per $4 \mu\text{m}^2$ for non-activated conditions (PLL) and activated conditions (2 or 8 min, anti-CD3/anti-CD28). Bars represent means \pm SD (B and F, top and center) or medians \pm interquartile range (B and F, bottom, as well as D) Tukey's ordinary one-way analysis of variance (ANOVA) (B and F, top and center) or Kruskal-Wallis (B and F, bottom, as well as D) multiple comparison tests; **** $p < 0.0001$; *** $p < 0.0005$; ** $p < 0.005$; ns, not significant. Data are from three independent experiments and represent thirty $4 \mu\text{m}^2$ regions obtained from 10–15 cells per condition. Scale bars represent 200 nm. See also Figure S3 and Tables S1–S3.

proposed by Jungmann et al. (2016) when using the qPAINT modality.

After identifying the clusters of single-molecule localizations using a well-established model-based Bayesian cluster analysis method (Griffié et al., 2017; Rubin-Delanchy et al., 2015) (color-outlined points in Figures 1C–1E, middle), and estimating the number of labeled proteins within that cluster using the previously described calibration, we used k-means clustering to assign localizations to each molecular target in the cluster and obtain a likely distribution of the underlying protein positions (Figures 1B–1E, bottom; Figure S2E). To assess the performance of k-means clustering in correctly assigning localizations to their molecular targets, we simulated a multimeric structure within the range of protein cluster density observed in the cell data (9 molecular targets in a $1,600 \text{ nm}^2$ area). We found that the accuracy of k-means clustering depends on the error of the single-molecule localizations with mis-assignments in the order of the median of the localization precision distribution, which for DNA-PAINT data typically range between 5 and 12 nm (Figures S2I–S2N). Although this level of accuracy is sufficient for our analysis, higher accuracy in position assignment can be achieved using more complex statistical analysis approaches (Fazel et al., 2019).

Overall, this approach allows the acquisition of multi-color stoichiometrically accurate maps of labeled protein positions with nanometer spatial precision. However, even if the number

of docking strands conjugated to the primary antibodies is ~ 1 , similar to any other technique that relies on antibody labeling, the final accuracy of our quantification toward absolute protein copy number is affected by the overall antibody-target binding efficiency, leading to potential undercounting. Nonetheless, by keeping the imaging and data processing conditions the same in all experiments, it is possible to compare and draw conclusions about changes in the spatial organization of the inspected proteins in the different conditions.

Nanoclusters of Csk, and Monomers of PAG, Are Recruited to the Plasma Membrane to Downmodulate Signaling

Using the quantitative approach described earlier, we reconstructed the distribution of Csk in T cells on surfaces coated with poly-L-lysine (PLL, control) and anti-CD3/anti-CD28 (activated) for either 2 or 8 min (Figure 2A, black and gray scatter points). When imaging under TIR excitation, the observed protein distribution encompasses a 2D projection of the 3D distribution of proteins located at the membrane (thickness of ~ 5 – 10 nm) and up to approximately 150 nm inside the cytosol. Therefore, we simultaneously observed both the membrane-associated Csk and the most proximal cytosolic Csk population to the plasma membrane.

To statistically quantify the observed spatial organization, we performed a second stage of Bayesian-based cluster analysis

on thirty $2 \times 2 \mu\text{m}^2$ protein map regions of interest (ROIs) from ten WT Jurkat T cells (Figures 2A and 2B). This analysis allowed us to quantify the total number of antibody-labeled Csk proteins, the number and size of Csk clusters, and the number of Csk proteins per cluster. The analysis showed that half of the total number of labeled Csk proteins are lost from the plasma membrane-proximal region following TCR engagement (17 ± 3 Csk proteins/ μm^2 compared with 31 ± 5 Csk proteins/ μm^2 in resting cells). At later time points, there is a re-recruitment of Csk to the membrane, even overshooting the original, resting protein density (43 ± 7 Csk proteins/ μm^2). The total Csk protein population is composed of two distinct pools: (1) unclustered Csk proteins, defined as Csk monomers, or (2) Csk proteins organized into clusters containing 9 ± 6 Csk proteins per cluster (Figure S3B).

Based on this, we assessed the differences between the two pools of Csk proteins (monomers or clusters) during TCR signaling. Immediately after TCR stimulation, there is a 54% decrease in the number of Csk clusters (0.8 ± 0.5 clusters/ μm^2) with respect to control conditions (1.6 ± 0.9 clusters/ μm^2) (Figure 2B). In late synapses, the number of Csk clusters increases dramatically (3.0 ± 0.7 clusters/ μm^2). Similar trends were observed by our group in naive and pre-stimulated primary human T cells imaged by dSTORM microscopy under TIR excitation, in which we detected that during late synapses, Csk clusters practically double with respect to non-activated conditions (Williamson et al., 2020). Conversely, the number of Csk monomers does not change substantially among resting (15 ± 4 proteins/ μm^2), early (11 ± 2 proteins/ μm^2), and late (17 ± 4 proteins/ μm^2) T cell synapses. Altogether, these data (summarized in Table S1) indicate that the early loss of membrane-proximal Csk and its re-recruitment at late times is dominated by the translocation of the clustered Csk pool, rather than the monomeric population.

Because the translocation of Csk is thought to be mediated by PAG and TRAF3, we then characterized the nanoscale organization of these proteins under the same conditions (Figures 2C–2F) (Kawabuchi et al., 2000; Wallis et al., 2017). We observed that concomitant with Csk late recruitment, the total number of antibody-labeled PAG proteins proximal to the TCR signalosome almost doubles following 8 min of TCR stimulation (from 9 ± 6 to 16 ± 6 PAG proteins/ μm^2) (Figures 2C and 2D). However, in contrast to the phenomena observed for Csk, PAG is predominantly recruited to the immune synapse as monomers and not as multi-protein assemblies, characterized by a 70% increase in the number of monomers with respect to control conditions (Table S2). In contrast, clustered PAG was unperturbed post-stimulation, with the number of PAG proteins per cluster and size of PAG clusters remaining unchanged (Figures S3E and S3F). However, we found that the overall amount of TRAF3 and its clustering behavior did not significantly change after CD3/CD28 stimulation (Figures 2E and 2F; Figures S3G–S3I; Table S3).

Monomeric, Not Clustered, PAG Mediates Csk Nanocluster Translocation

Many receptors and signaling molecules co-localize into micro- and nanoscale domains during T cell activation (Sherman et al., 2013). However, there is a lack of statistical tools to study these

nanosized multivalent clusters. Most analysis techniques focus on 2-color co-localization clustering analysis and are based on extracting a Pearson's correlation coefficient from the comparison between the clustering of self-localizations and the clustering relative to the other protein species (Malkusch et al., 2012; Rossy et al., 2014). Still, these methods are difficult to generalize to higher-color data.

We therefore combined multi-color, stoichiometric super-resolution localization microscopy with Bayesian-based clustering and new co-localization analysis tools to describe the formation of mixed signaling complexes of Csk, PAG, and TRAF3 in T cells. Our multivalent cluster analysis method is based on quantifying the number and composition of mixed clusters and statistically comparing the significance of the results with the case of coincidental co-localization. Deviation of the number of mixed signaling clusters found in the experimental dataset from a generated, randomly shuffled dataset (more details given later) indicates that there is indeed either mixed protein clustering or preferred protein segregation within the data. However, if there are no significant differences between the two datasets, then we can conclude that the detected cluster combination or combinations are not significant.

The pipeline of the method is as follows. First, we generated three-color protein maps by assigning a unique pseudo-color to each species and by aligning and combining each color image using gold nanoparticles as fiducial markers (Figure 3A, top). Bayesian cluster analysis was performed on the color-coded combined protein maps of thirty ROIs from ten Jurkat T cells. Besides retrieving the typical cluster characteristic parameters, we obtained the information related to the protein composition of each cluster (Figure 3A, bottom) and plotted it in ternary composition diagrams (Figure 3B). Every point on the ternary plot represents a different composition of the three components: Csk (red), TRAF3 (green), and PAG (blue) (Figure S4A). Specifically, we assigned to each cluster a color code that correlates to the percentage of each protein in the cluster (Figure 3B) and depicted four circles that correspond to the four possible cluster combinations: (1) Csk-TRAF3, (2) Csk-PAG, (3) PAG-TRAF3, and (4) Csk-TRAF3-PAG. The color and position of each of these circles relate to the most prominent composition of each cluster combination, and the size represents the percentage of that cluster combination in relation to the others.

Ternary graphs for Csk-TRAF3-PAG indicate that Csk co-clusters with TRAF3 and PAG proteins to a greater extent than any other protein combinations (PAG-TRAF3 and Csk-TRAF3-PAG), with PAG-TRAF3 co-clusters only contributing to a minority of mixed protein clusters. To quantify the amount of co-clustering, which could be the result of coincidental co-localization, and therefore assess the degree of significance of the detected Csk-PAG and Csk-TRAF3 clusters, we shuffled the thirty individual ROIs of Csk, PAG, and TRAF3 protein maps in each condition and created new merged maps of Csk, PAG, and TRAF3 from randomly selected ROIs. We then analyzed the shuffled maps using the same pipeline as described earlier (Figure S4B). The number of mixed clusters of the different cluster combinations (Csk-PAG, Csk-TRAF3, and PAG-TRAF3) was then counted in each ROI for the different experimental conditions (PLL, 2 or 8 min) and compared with its

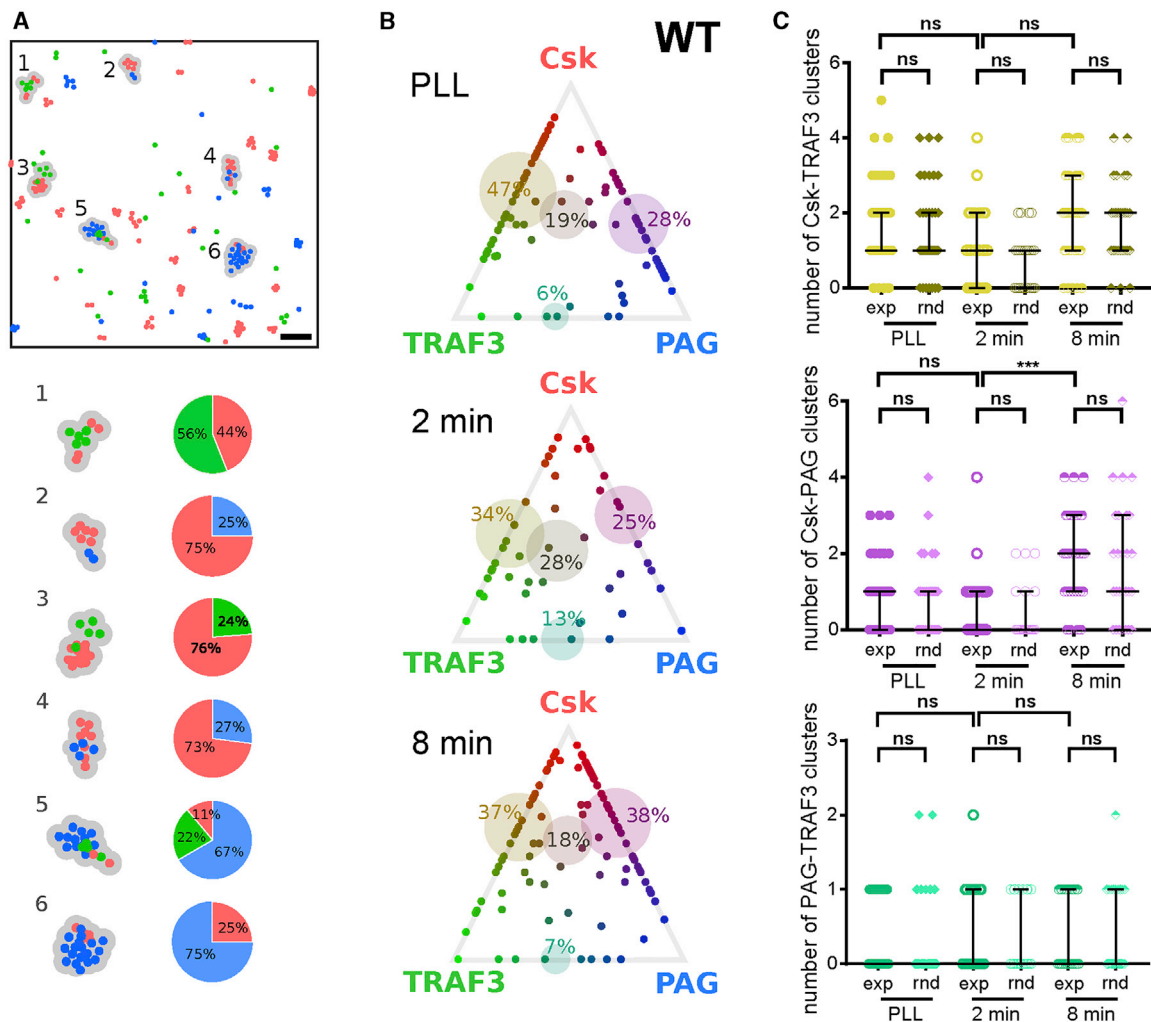


Figure 3. Csk, PAG, and TRAF3 Mixed Protein Cluster Analysis

(A) Three pseudo-color protein map distributions (points) of Csk (red), PAG (blue), and TRAF3 (green) in WT Jurkat T cells supported on PLL were analyzed with a Bayesian-based cluster analysis algorithm to identify mixed protein cluster points (gray outlined) in $4 \mu\text{m}^2$ region maps (center, boxed region).

(B) Composition (A) of each identified cluster was calculated (bottom), and results (B) for WT Jurkat T cells supported on glass coated with PLL (top) or anti-CD3/anti-CD28 for either 2 min (center) or 8 min (bottom) were plotted in ternary diagrams. Each point represents a mixed cluster; the position and color of the point decode its protein composition. The four main cluster combinations (i.e., Csk-PAG, Csk-TRAF3, PAG-TRAF3, and Csk-PAG-TRAF3) are represented by a transparent circle positioned in the most likely cluster composition for that combination, with the size representing the contribution of that cluster combination type with respect to all found mixed clusters.

(C) To evaluate the significance of the detected merged clusters, numbers of identified mixed clusters for Csk-TRAF3 (top), Csk-PAG (center), and PAG-TRAF3 (bottom) in experimental (exp) data are compared with the random case (rnd). Bars represent medians \pm interquartile range. Kruskal-Wallis multiple comparison nonparametric test; *** $p < 0.0005$; * $p < 0.05$; ns, not significant.

Data are from three independent experiments and represent thirty $4 \mu\text{m}^2$ regions obtained from 10–15 cells per condition. Scale bar in (A) represents 200 nm. See also Figure S3.

corresponding shuffled dataset (Figure 3C, exp [experimental] versus rnd [random]).

This controlled assessment allowed us to conclude that even the detected Csk-PAG or PAG-TRAF3 cluster combinations do not show additional, specific co-clustering above that expected for the random case. In particular, we ascribe the observed increase in the number of Csk-PAG clusters during late synapses to the higher density of Csk and PAG proteins at that time point (8 min of TCR stimulation), which increases the

probability (~ 2 times higher) of randomly detecting Csk and PAG proteins in the same region of the space (Figure 3C, middle). This indicates that the Csk-PAG interaction does not involve the pool of clustered PAG at the plasma membrane, either before or after TCR stimulation. This is in keeping with our finding that only the monomeric pool of PAG changes following TCR activation. With regards to TRAF3, we did not observe significant evidence to infer that TRAF3 clusters mediate Csk nanocluster translocation from the membrane

to the cytosol, because no significant TRAF3-Csk co-clustering was detected.

PTPN22 Is Required to Re-recruit Csk to Late Synapses

Csk is known to be one of the main interaction partners of PTPN22, a key downregulator of TCR signaling that can dephosphorylate Lck on its active residue, Tyr³⁹⁴ (Cloutier and Veillette, 1999). PTPN22 and Csk form a complex that is thought to enable synergistic inhibition of TCR signaling (Cloutier and Veillette, 1999; Gjørloff-Wingren et al., 1999; Veillette et al., 2009). However, other reports suggest that the PTPN22-Csk complex limits PTPN22 function by either restraining its localization to the cytoplasm (Vang et al., 2012) or promoting the phosphorylation of an inhibitory residue on PTPN22 (de la Puerta et al., 2013). Here, we exploit the high sensitivity of DNA-PAINT, combined with our cluster and co-cluster analysis pipeline, to enable for the first time a detailed study of how the loss of PTPN22 affects Csk regulatory function.

Recently, we demonstrated the first example of an isogenic human T cell line that lacks PTPN22 generated using CRISPR gene editing (Bray et al., 2018). We confirmed by western blotting the complete suppression of PTPN22 expression while maintaining constant expression levels of known PTPN22 interactors Lck, Zap-70, and Csk, as well as PAG and TRAF3 (Figure 4A) (Bray et al., 2018). PTPN22 KO Jurkat T cells exhibit, in response to TCR stimulation, increased ERK phosphorylation (Figure 4B) and interleukin-2 (IL-2) expression levels (Bray et al., 2018). As expected, we do not detect phosphorylation differences in upstream signaling molecules such as Lck and ZAP-70 between WT and PTPN22 KO cells (Figure S5).

In contrast to whole-cell level results (Figure 4A), using DNA-PAINT, we observed a 46% increase in the total amount of Csk at the membrane with respect to WT cells (Figures 4C and 4D). This increase is mainly dictated by the higher number of Csk clusters in PTPN22 KO cells (2.5 ± 1.0 Csk clusters/ μm^2) with respect to WT cells (1.6 ± 0.9 Csk clusters/ μm^2), with almost no increase from the monomeric pool of Csk (15 ± 4 Csk proteins/ μm^2 in WT versus 18 ± 4 Csk proteins/ μm^2 in PTPN22 KO) (p values for WT and KO comparisons are $p < 0.0001$ and $p < 0.0410$, respectively). As was the case for the WT cells, following TCR stimulation, these Csk clusters are lost; however, the reduction is somewhat smaller when compared with WT cells (54% reduction in WT versus 35% in PTPN22 KO). Most interestingly, the absence of PTPN22 leads to a marked failure to re-recruit Csk clusters to the plasma membrane during late synapses. In the KO condition, the number of Csk clusters at late synapses is 20% lower (2.0 ± 1.0 Csk clusters/ μm^2) than in resting cells (2.5 ± 1.0 Csk clusters/ μm^2). Furthermore, there are no significant differences ($p > 0.9999$) in the number of clusters detected at early and late synapses, in contrast to the behavior observed in the WT cells, in which the number of Csk clusters quadrupled between early and late activation ($p < 0.0001$). Finally, the cluster characteristics of Csk—i.e., the number of proteins per cluster and the cluster size—in PTPN22 KO cells are similar to those in WT cells (Figures S3A–S3C). Altogether, these data indicate that PTPN22 regulates the relative levels of Csk clusters proximal to the plasma membrane by controlling the amount of Csk

clusters that migrates there from the cytosol during late synapses.

PAG Late Recruitment Is Also Disrupted in the Absence of PTPN22

We also examined the effect of PTPN22 deficiency on the nano-scale organization of PAG and TRAF3. Like Csk, PAG in PTPN22 KO cells showed markedly different behavior in comparison to WT cells. PAG density and clustering before and after TCR stimulation showed no significant differences in the absence of PTPN22 (Figures 4E and 4F). However, PAG did display higher basal levels (15 ± 7 PAG proteins/ μm^2) throughout the time course used in this study, even though PAG expression levels at the whole-cell level were equivalent for both WT and PTPN22 KO cells (Figure 4A). With respect to TRAF3 (Figures 4G and 4H), total TRAF3 at the plasma membrane is higher in PTPN22 KO cells compared with WT (15 ± 4 versus 12 ± 4 TRAF3 proteins/ μm^2) ($p = 0.0149$). Again, these results contrast with whole-cell biochemical experiments (Figure 4A) in that we did not observe any difference for TRAF3 expression level between WT and PTPN22 KO cells. Absence of PTPN22 therefore causes a failure to re-recruit Csk at late time points, a failure to recruit PAG, and an overabundance of TRAF3 at the plasma membrane. To assess the existence of mixed Csk, PAG, and TRAF3 clusters in PTPN22 KO cells, we used the same pipeline as described earlier (Figures S4C and S4D). Unlike for WT cells, we found that the detection of Csk and TRAF3 mixed clusters in resting cells is significant ($p = 0.0335$) and that they separate immediately after activation (Figure S4E).

DISCUSSION

Translocation of Csk to the plasma membrane by transmembrane adaptor proteins, such as PAG, is a critical step toward Src kinase inactivation of the T cell signaling pathway through phosphorylation of the Lck inhibitory tyrosine site. In resting T cells, PAG is constitutively phosphorylated at Tyr³¹⁷, enabling binding of Csk through its SH2 domain (Brdička et al., 2000). However, upon T cell stimulation, PAG becomes dephosphorylated, allowing Csk to translocate to the cytoplasm, and as such, it alleviates Csk inhibition on active Lck. CD45 has been identified as one of the main phosphatase of PAG (Davidson et al., 2003). Therefore, the exact timing of CD45 exclusion from the engaged TCRs will correlate with the initial loss of Csk from the plasma membrane. Razvag et al. (2018) showed, via live-cell SMLM, that kinetic segregation occurs within seconds from TCR activation, yet CD45 is not removed too far from the TCRs for optimal activation within clusters. Their data indicate that CD45 remains in close contact to dephosphorylate and fully activate Lck before being segregated from the closed-contact membrane between the T cell and the antigen-presenting cell. They observed that CD45 leaves a depletion zone of ~ 250 nm within a few dozen seconds after the initial adhesion. Therefore, we speculate that similar timing might operate for the dephosphorylation of PAG by CD45, the concurrent loss of membrane-associated Csk, and the full activation of Lck by freeing it from Csk's inhibitory action. These timescales align well with biochemical assays that showed a 75% reduction of the PAG-

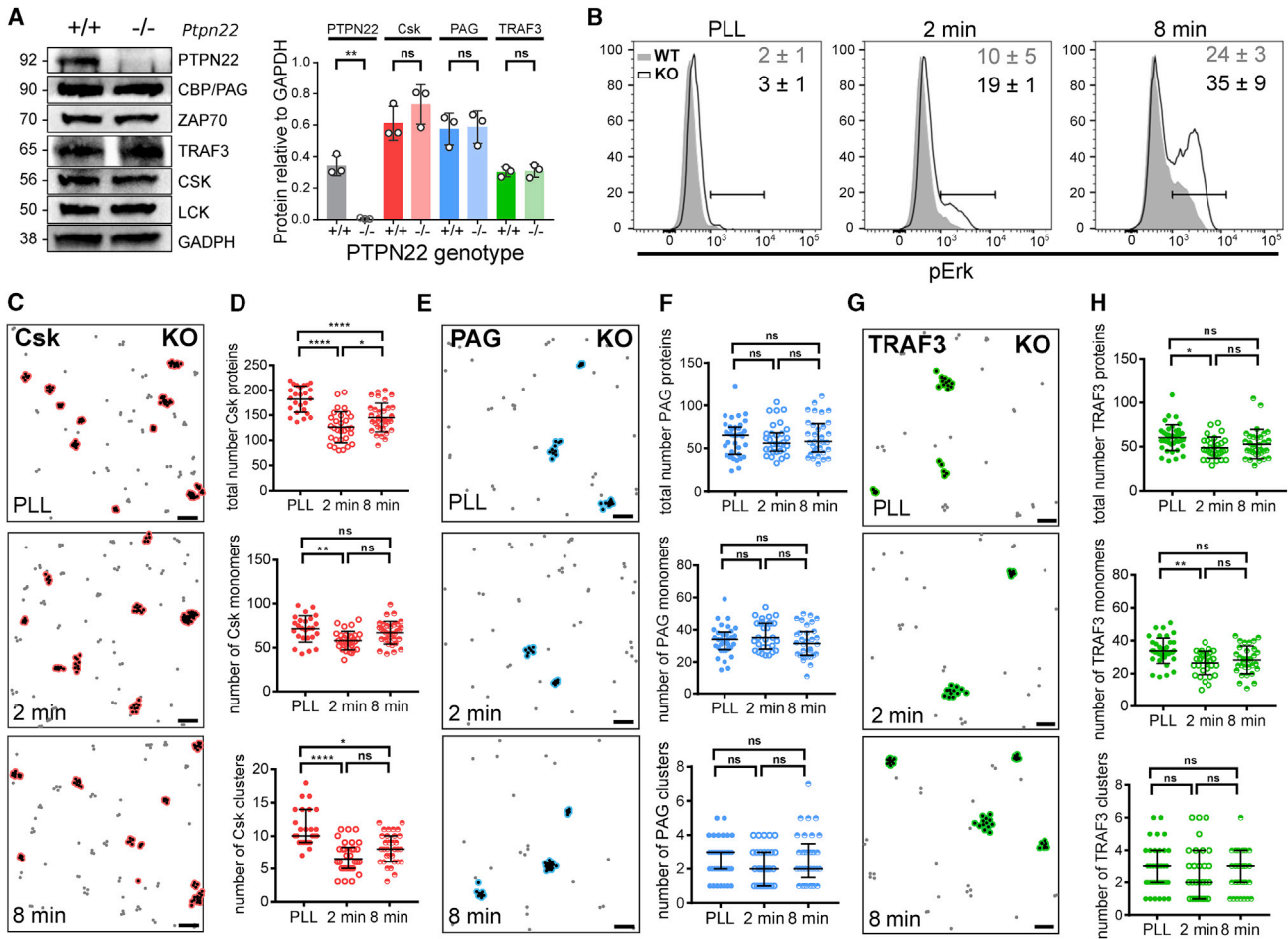


Figure 4. Csk and PAG Recruitment at Late Synapses Is Impaired in PTPN22 KO T Cells

(A) WT and PTPN22 KO T cells were lysed and analyzed by western blotting against the indicated proteins. Protein abundance relative to GAPDH in non-stimulated cells was determined. Bars represent means \pm SD of three experiments. Tukey's ordinary one-way ANOVA; ** $p = 0.0029$; ns, not significant.

(B) WT (gray) and PTPN22 KO (white) T cells were supported on glass coated with PLL or anti-CD3/anti-CD28 for either 2 or 8 min before undergoing flow cytometric analysis of Erk phosphorylation. The values represent the percentage of cells that are pErk positive. Data are representative of 3 independent experiments.

(C–H) Csk (C), PAG (E), and TRAF3 (G) protein maps reconstructed from the DNA-PAINT localization maps of PTPN22 KO Jurkat T cells supported on glass coated with PLL (top) or anti-CD3/anti-CD28 for either 2 min (center) or 8 min (bottom) were analyzed using a Bayesian-based cluster analysis to identify cluster points (red or blue outlined) and extract their properties. Scale bars represent 200 nm. Selected descriptors from the cluster analysis of Csk (D), PAG (F), and TRAF3 (H) protein maps representing total number of proteins (top), number of non-clustered proteins (center), and number of clusters (bottom) per $4 \mu\text{m}^2$ for PLL or 2- or 8-min anti-CD3/anti-CD28. Bars represent means \pm SD (D and H, top and center) or medians \pm interquartile range (D and H, bottom, and F). Tukey's ordinary one-way ANOVA (D and H, top and center) or Kruskal-Wallis (D and H, bottom, and F) multiple comparison tests; **** $p < 0.0001$; ** $p < 0.005$; * $p < 0.05$; ns, not significant.

Data are from three independent experiments and represent thirty $4 \mu\text{m}^2$ regions obtained from 10–15 cells per condition. See also [Figures S3–S5](#) and [Tables S1–S3](#).

bound Csk population after the first 0.5 min of TCR engagement, with the dissociation being essentially complete within the first 2 min (Davidson et al., 2016). However, Csk late re-recruitment to the plasma membrane is also associated with PAG rephosphorylation and happens after 5–7 min of TCR engagement (Brdicka et al., 2000; Torgersen et al., 2001). Therefore, we specifically choose to analyze Csk nanoscale organization after 2- and 8-min anti-CD3 + anti-CD28 stimulation as suitable snapshot models for the case of Csk lost and re-recruitment from and to lipid rafts, respectively.

To obtain a snapshot picture of Csk distribution in non-activating conditions, we opted to use Jurkat T cells supported on surfaces coated with PLL. In contrast to Santos et al. (2018) that generated controversy about whether a true resting condition can be observed when a T cell interacts with a PLL-coated surface, we have two sets of independent evidence that point to how, in our experiments, T cells deposited on PLL surfaces are not activated compared with actual activating conditions (glass slides coated with anti-CD3 + anti-CD28). The first one is the flow cytometric analysis data of Erk phosphorylation

(which indicates successful signal transduction from TCR to the end) presented in Figure 4B, showing that only $2\% \pm 1\%$ and $3\% \pm 1\%$ of WT and PTPN22 KO Jurkat T cells, respectively, deposited on PLL surfaces are pERK positive. In contrast, these values increase to $10\% \pm 5\%$ and $19\% \pm 1\%$ and to $24\% \pm 3\%$ and $35\% \pm 9\%$ for WT and PTPN22 KO T cells supported on glass coated with anti-CD3/anti-CD28 for 2- and 8-min stimulation, respectively. Furthermore, we observed that Jurkat T cells form a smaller footprint (contact area) on PLL-coated slides compared with slides coated with anti-CD3/anti-CD28 (Figure S1; Table S4). In conclusion, our experimental results point to how Jurkat T cells did not undergo substantial activation on PLL surfaces, and as such, they represent a good model for examining the distribution of signaling clusters in resting conditions.

We found that Csk exists in clusters proximal to and/or at the plasma membrane and that those clusters briefly leave the TCR signalosome following early (2 min) TCR stimulation to later (8 min) return to restore its regulatory function. The translocation of Csk clusters to the cytosol enhances the efficacy of downstream signaling by freeing Lck from Csk's inhibitory action. The re-recruitment of the cytosolic Csk to the membrane is therefore crucial to its function (Otáhal et al., 2011). The transmembrane adaptor PAG has long been proposed to mediate membrane recruitment of Csk via its SH2 domain (Brdička et al., 2000). Our data show that although no significant mixed Csk-PAG clusters exist, the density of both molecules increases at the immune-synapse area during late signaling, with the number of PAG monomers almost doubling. Notably, there is a 1 to ~ 1.5 ratio of PAG to Csk monomers after 8 min of TCR signaling stimulation. These observations tend to support that PAG and Csk proteins bind in a 1:1 stoichiometry and that although Csk clusters are not directly associated with PAG, they might provide a readily accessible pool of Csk proteins close to the plasma membrane for PAG interaction.

However, we cannot rule out the possibility that some percentage of Csk proteins (either monomers or clusters) is associated with other transmembrane proteins. Although PAG is the most studied transmembrane protein known to control Csk association and dissociation from lipid rafts at the plasma membrane, LIME (Lck-interacting membrane protein) has also been suggested to regulate T cell activation by recruiting Csk to the lipid rafts (Brdicková et al., 2003). In addition, experiments with membrane-raft-targeted Csk constructs showed that Csk exerted the same level of inhibition independent of whether this motif was derived from Lck, Fyn, LAT, or PAG, suggesting that additional adaptors could bring Csk to membrane rafts (Otáhal et al., 2011). These observations are supported by PAG/Cbp and LIME KO mice experiments in which no apparent deregulation of TCR signaling was observed (Dobenecker et al., 2005; Xu et al., 2005). Whether Csk binds only to PAG or to other transmembrane proteins to exert its inhibitory action on the TCR signalosome remains to be confirmed and is beyond the focus of our work.

We quantified that Csk clusters contain 9 ± 6 Csk proteins, with cluster radius ranging from 18 to 32 nm. This range of cluster parameters agrees well with other signaling molecules, such as TCR (7–30 TCRs per cluster with a 35- to 70-nm cluster radius)

(Lillemeier et al., 2010) or CD59 (3–9 CD59 glycoproteins per cluster) (Suzuki et al., 2007) as determined by transmission electron microscopy (TEM) or single-molecule tracking experiments, respectively. Furthermore, they are in line with computational and systems biology approaches that have revealed that cluster size in the range of ~ 5 –10 molecules allows higher signal fidelity (Roob et al., 2016).

We also investigated the role of PTPN22 in Csk clustering dynamics. PTPN22, a key downregulator of TCR signaling that can dephosphorylate Lck in its active Tyr³⁹⁴ residue, is a phosphatase of interest because of a missense mutation (R620W) that has been linked to more than 16 autoimmune diseases in humans, including type 1 diabetes, rheumatoid arthritis, and systemic lupus erythematosus (Siminovitch, 2004; Stanford and Bottini, 2014). The C1858T single-nucleotide polymorphism in PTPN22 disrupts its interaction site with Csk (Bottini et al., 2004). However, the functional outcomes associated with PTPN22-Csk-impaired association remained unclear, because both gain and loss of phosphatase function have been reported for the PTPN22-R620W variant in humans (Vang et al., 2005, 2018; Zikherman et al., 2009). By isolating the effect of PTPN22 from the inherent complications in analyzing human data (i.e., genetic and environmental variables of distinct individuals), we found that absence of PTPN22 leads to increased ERK phosphorylation and IL-2 expression, which is in keeping with the loss-of-function results observed for the PTPN22 KO (Hasegawa et al., 2004) and the orthologous R619W allelic variant in mouse T cells (Zhang et al., 2011).

We detected that in the PTPN22 KO cells there is a marked failure to recruit back Csk and PAG during late synapses, as well as failure to lose Csk following early TCR engagement. PTPN22 is therefore required to maintain membrane-proximal Csk clusters. Quantitative proteomics experiments and co-immunoprecipitation results reveal that the PTPN22-Csk association is constitutive: it decreases following TCR stimulation, reaching a maximum after ~ 10 min of TCR stimulation (de la Puerta et al., 2013; Voisinne et al., 2019). This might indicate that Csk clustering deregulation in PTPN22 KO cells is linked to the loss of Csk-PTPN22 interaction. For example, Davidson et al. (2016) indicated that PTPN22 and Dok adaptors cooperate with PAG to recruit Csk to the plasma membrane to interact with different Src kinases, so it is possible that PTPN22 might bring Csk to the tyrosine-phosphorylated ITAMs and ZAP-70. In contrast to the results observed in WT cells, we also detected that lack of PTPN22 leads to a modest formation of mixed Csk and TRAF3 clusters in resting T cells and that there is a slight increase in TRAF3 total expression levels that evens out to WT levels following TCR engagement. It is possible that in the absence of PTPN22, TRAF3—which otherwise would be bound to PTPN22 and Csk, enhancing their interaction in the cytoplasm (Wallis et al., 2017)—is only interacting with Csk, leading to increased co-localization.

In conclusion, we propose a model (Figure 5) in which Csk nanoclusters are central to increasing the effective avidity to membrane-associated proteins, in which Csk can exert its inhibitory function on Src family kinases. In this view, Csk clusters provide both an instant pool of Csk monomers and a quick

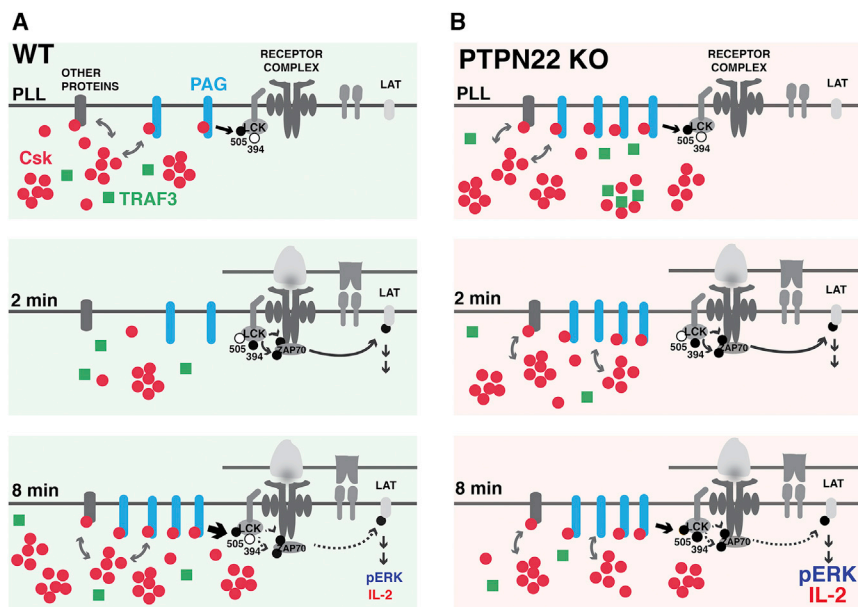


Figure 5. Csk Clusters Proximal to the Plasma Membrane Deliver Csk Monomers to Downregulate Signaling in a PTPN22-Dependent Manner

(A) Csk exerts tonic inhibitory control of TCR signaling by promoting the closed and inactive conformation of Src family kinases, such as Lck, via phosphorylation of its regulatory sites (top). Immediately after T cell activation, Csk clusters move away from the plasma membrane, which leads to activation of Lck and initiation of the TCR phosphorylation cascade (middle). To curtail prolonged T cell activation, Csk clusters are recruited back en masse to the plasma membrane to deliver Csk monomers to late-recruited PAG (bottom). However, TRAF3 clusters are not involved in the translocation of Csk clusters from the plasma membrane to the cytoplasm, and vice versa.

(B) Csk and PTPN22 form a complex that modulates the inhibitory function of both proteins in TCR signaling. Loss of PTPN22 leads to impaired Csk clustering dynamics with augmented Csk and PAG expression levels close to the TCR signalosome. Late recruitment of Csk clusters to the plasma membrane is impaired, and PAG appears to be constitutively recruited in PTPN22 KO cells (bottom). As a consequence, TCR signaling is augmented and sustained compared with WT T cells.

means to exclude Csk proteins from the TCR signalosome to account for proper activation. By excluding Csk nanoclusters from the membrane-proximal area, the activation kinase cascade can be sensitive to changes in the localization of only a few ligands. These results can help inform the increasingly complex mathematical models derived to explain TCR signal discrimination through the kinetic proofreading model, in which high receptor signaling fidelity is a consequence of introducing delays, via numerous feedback and feedforward interactions of signaling proteins, between the ligand binding event and the commitment of the signaling machinery to an activated state. Furthermore, our model is consistent with experimental evidence from other groups showing that a modest decrease in Csk levels is sufficient to increase Lck phosphorylation on its activating residue, Tyr³⁹⁴ (Manz et al., 2015). Consistently, by comparing the results in WT and PTPN22 KO cells, we identified that even small changes in the total number of Csk molecules, which would be difficult to detect with current biochemical methods, are enough to provoke increase in functional readouts, such as IL-2 and Erk phosphorylation levels. Overall, our results illustrate the power of DNA-PAINT, when combined with the latest statistical cluster and co-cluster analysis frameworks, to dissect complex signaling pathways that are regulated by nanoscale spatiotemporal organization.

STAR★METHODS

Detailed methods are provided in the online version of this paper and include the following:

- KEY RESOURCES TABLE

● RESOURCE AVAILABILITY

- Lead Contact
- Materials Availability
- Data and Code Availability

● EXPERIMENTAL MODELS AND SUBJECT DETAILS

● METHOD DETAILS

- Antibodies and DNA
- DNA-antibody coupling reaction
- Western blotting
- Phospho flow cytometry
- Immunofluorescence staining
- T cell imaging conditions
- Reconstruction of proteins maps and data analysis
- Mixed protein cluster analysis
- Calibration of DNA-PAINT imaging
- 2D DNA-origami simulations and analysis
- 2D DNA-origami calibration sample and analysis

● QUANTIFICATION AND STATISTICAL ANALYSIS

SUPPLEMENTAL INFORMATION

Supplemental Information can be found online at <https://doi.org/10.1016/j.celrep.2020.108523>.

ACKNOWLEDGMENTS

This work has been supported by BBSRC grant BB/R007365/1 and Versus Arthritis grant 20525. S.S. acknowledges financial support from the Human Frontier Science Program Organization and the Royal Society through HFSP (LT001463/2017-C) and Dorothy Hodgkin (DHF/R1\191019) fellowships, respectively. R.Z. acknowledges funding from Wellcome Trust Investigator Award WT25014/Z/16/Z. We acknowledge the use of the Nikon Imaging Facility (NIC) at King's College London for data acquisition.

AUTHOR CONTRIBUTIONS

S.S. prepared the DNA-coupled primary antibodies, performed the Exchange-PAINT imaging experiments, developed relevant analysis code, analyzed data, and wrote the manuscript. J.G. developed clustering and co-clustering analysis code. D.J.W. generated samples. J.B. performed the western blotting and the flow cytometry experiments. C.B. generated the CRISPR-Cas9-mediated PTPN22 deletion, and R.Z. supervised the PTPN22 KO Jurkat T cell construction. D.M.O. and A.P.C. conceived the idea and supervised the research. All authors provided feedback on the manuscript.

DECLARATION OF INTERESTS

The authors declare no competing interests.

Received: February 17, 2020

Revised: July 7, 2020

Accepted: November 24, 2020

Published: December 22, 2020

REFERENCES

- Baumgart, F., Arnold, A.M., Leskovar, K., Staszek, K., Fölser, M., Weghuber, J., Stockinger, H., and Schütz, G.J. (2016). Varying label density allows artifact-free analysis of membrane-protein nanoclusters. *Nat. Methods* *13*, 661–664.
- Bergman, M., Mustelin, T., Oetken, C., Partanen, J., Flint, N.A., Amrein, K.E., Autero, M., Burn, P., and Aitalo, K. (1992). The human p50csk tyrosine kinase phosphorylates p56lck at Tyr-505 and down regulates its catalytic activity. *EMBO J.* *11*, 2919–2924.
- Betzig, E., Patterson, G.H., Sougrat, R., Lindwasser, O.W., Olenych, S., Bonifacio, J.S., Davidson, M.W., Lippincott-Schwartz, J., and Hess, H.F. (2006). Imaging intracellular fluorescent proteins at nanometer resolution. *Science* *313*, 1642–1645.
- Bottini, N., Musumeci, L., Alonso, A., Rahmouni, S., Nika, K., Rostamkhani, M., MacMurray, J., Meloni, G.F., Lucarelli, P., Pellicchia, M., et al. (2004). A functional variant of lymphoid tyrosine phosphatase is associated with type I diabetes. *Nat. Genet.* *36*, 337–338.
- Bray, C., Wright, D., Haupt, S., Thomas, S., Stauss, H., and Zamoyska, R. (2018). Crispr/Cas mediated deletion of PTPN22 in Jurkat T cells enhances TCR signaling and production of IL-2. *Front. Immunol.* *9*, 2595.
- Brdička, T., Pavlistová, D., Leo, A., Bruyns, E., Korínek, V., Angelisová, P., Scherer, J., Shevchenko, A., Hilgert, I., Cerný, J., et al. (2000). Phosphoprotein associated with glycosphingolipid-enriched microdomains (PAG), a novel ubiquitously expressed transmembrane adaptor protein, binds the protein tyrosine kinase csk and is involved in regulation of T cell activation. *J. Exp. Med.* *191*, 1591–1604.
- Brdicková, N., Brdīčka, T., Angelisová, P., Horváth, O., Špička, J., Hilgert, I., Pačes, J., Simeoni, L., Kliche, S., Merten, C., et al. (2003). LIME: a new membrane Raft-associated adaptor protein involved in CD4 and CD8 coreceptor signaling. *J. Exp. Med.* *198*, 1453–1462.
- Cloutier, J.F., and Veillette, A. (1999). Cooperative inhibition of T-cell antigen receptor signaling by a complex between a kinase and a phosphatase. *J. Exp. Med.* *189*, 111–121.
- Dai, M., Jungmann, R., and Yin, P. (2016). Optical imaging of individual biomolecules in densely packed clusters. *Nat. Nanotechnol.* *11*, 798–807.
- Davidson, D., Bakinowski, M., Thomas, M.L., Horejsi, V., and Veillette, A. (2003). Phosphorylation-dependent regulation of T-cell activation by PAG/Cbp, a lipid raft-associated transmembrane adaptor. *Mol. Cell. Biol.* *23*, 2017–2028.
- Davidson, D., Zhong, M.C., Pandolfi, P.P., Bolland, S., Xavier, R.J., Seed, B., Li, X., Gu, H., and Veillette, A. (2016). The Csk-Associated Adaptor PAG Inhibits Effector T Cell Activation in Cooperation with Phosphatase PTPN22 and Dok Adaptors. *Cell Rep.* *17*, 2776–2788.
- de la Puerta, M.L., Trinidad, A.G., Rodríguez, Mdel.C., de Pereda, J.M., Sánchez Crespo, M., Bayón, Y., and Alonso, A. (2013). The autoimmunity risk variant LYP-W620 cooperates with CSK in the regulation of TCR signaling. *PLoS ONE* *8*, e54569.
- Dobenecker, M.-W., Schmedt, C., Okada, M., and Tarakhovskiy, A. (2005). The ubiquitously expressed Csk adaptor protein Cbp is dispensable for embryogenesis and T-cell development and function. *Mol. Cell. Biol.* *25*, 10533–10542.
- Fazel, M., Wester, M.J., Rieger, B., Jungmann, R., and Lidke, K.A. (2019). Sub-Nanometer Precision using Bayesian Grouping of Localizations. *bioRxiv*. <https://doi.org/10.1101/752287>.
- Feher, K., Halstead, J.M., Goyette, J., and Gaus, K. (2019). Can single molecule localization microscopy detect nanoclusters in T cells? *Curr. Opin. Chem. Biol.* *51*, 130–137.
- Gjörloff-Wingren, A., Saxena, M., Williams, S., Hammi, D., and Mustelin, T. (1999). Characterization of TCR-induced receptor-proximal signaling events negatively regulated by the protein tyrosine phosphatase PEP. *Eur. J. Immunol.* *29*, 3845–3854.
- Griffié, J., Shannon, M., Bromley, C., Boelen, L., Burn, G.L., Williamson, D.J., Heard, N.A., Cope, A.P., Owen, D.M., and Rubin-Delanchy, P. (2016). A Bayesian cluster analysis method for single-molecule localization microscopy data. *Nature Protocols* *11*, 2499–2514.
- Griffié, J., Shlomovich, L., Williamson, D.J., Shannon, M., Aaron, J., Khuon, S., L Burn, G., Boelen, L., Peters, R., Cope, A.P., et al. (2017). 3D Bayesian cluster analysis of super-resolution data reveals LAT recruitment to the T cell synapse. *Sci. Rep.* *7*, 4077.
- Griffié, J., Burn, G.L., Williamson, D.J., Peters, R., Rubin-Delanchy, P., and Owen, D.M. (2018). Dynamic Bayesian Cluster Analysis of Live-Cell Single Molecule Localization Microscopy Datasets. *Small Methods* *2*, 1800008.
- Hasegawa, K., Martin, F., Huang, G., Tumas, D., Diehl, L., and Chan, A.C. (2004). PEST domain-enriched tyrosine phosphatase (PEP) regulation of effector/memory T cells. *Science* *303*, 685–689.
- Hrdinka, M., and Horejsi, V. (2014). PAG—a multipurpose transmembrane adaptor protein. *Oncogene* *33*, 4881–4892.
- Jungmann, R., Steinhauer, C., Scheible, M., Kuzyk, A., Tinnefeld, P., and Simmel, F.C. (2010). Single-molecule kinetics and super-resolution microscopy by fluorescence imaging of transient binding on DNA origami. *Nano Lett.* *10*, 4756–4761.
- Jungmann, R., Avendaño, M.S., Woehrstein, J.B., Dai, M., Shih, W.M., and Yin, P. (2014). Multiplexed 3D cellular super-resolution imaging with DNA-PAINT and Exchange-PAINT. *Nat. Methods* *11*, 313–318.
- Jungmann, R., Avendaño, M.S., Dai, M., Woehrstein, J.B., Agasti, S.S., Feiger, Z., Rodal, A., and Yin, P. (2016). Quantitative super-resolution imaging with qPAINT. *Nat. Methods* *13*, 439–442.
- Katz, Z.B., Novotná, L., Blount, A., and Lillemeier, B.F. (2017). A cycle of Zap70 kinase activation and release from the TCR amplifies and disperses antigenic stimuli. *Nat. Immunol.* *18*, 86–95.
- Kawabuchi, M., Satomi, Y., Takao, T., Shimonishi, Y., Nada, S., Nagai, K., Tarakhovskiy, A., and Okada, M. (2000). Transmembrane phosphoprotein Cbp regulates the activities of Src-family tyrosine kinases. *Nature* *404*, 999–1003.
- Lee, S.H., Shin, J.Y., Lee, A., and Bustamante, C. (2012). Counting single photoactivatable fluorescent molecules by photoactivated localization microscopy (PALM). *Proc. Natl. Acad. Sci. USA* *109*, 17436–17441.
- Lillemeier, B.F., Mörtelmaier, M.A., Forstner, M.B., Huppa, J.B., Groves, J.T., and Davis, M.M. (2010). TCR and Lat are expressed on separate protein islands on T cell membranes and concatenate during activation. *Nat. Immunol.* *11*, 90–96.
- Malkusch, S., Endesfelder, U., Mondry, J., Gelléri, M., Verveer, P.J., and Heilemann, M. (2012). Coordinate-based colocalization analysis of single-molecule localization microscopy data. *Histochem. Cell Biol.* *137*, 1–10.
- Manz, B.N., Tan, Y.X., Courtney, A.H., Rutaganira, F., Palmer, E., Shokat, K.M., and Weiss, A. (2015). Small molecule inhibition of Csk alters affinity recognition by T cells. *eLife* *4*, e08088.

- Nada, S., Yagi, T., Takeda, H., Tokunaga, T., Nakagawa, H., Ikawa, Y., Okada, M., and Aizawa, S. (1993). Constitutive activation of Src family kinases in mouse embryos that lack Csk. *Cell* **73**, 1125–1135.
- Nieuwenhuizen, R.P.J., Bates, M., Szymborska, A., Lidke, K.A., Rieger, B., and Stallinga, S. (2015). Quantitative localization microscopy: effects of photophysics and labeling stoichiometry. *PLoS ONE* **10**, e0127989.
- Otáhal, P., Pata, S., Angelisová, P., Horejší, V., and Brdička, T. (2011). The effects of membrane compartmentalization of csk on TCR signaling. *Biochim. Biophys. Acta* **1813**, 367–376.
- Razvag, Y., Neve-Oz, Y., Sajman, J., Rechtes, M., and Sherman, E. (2018). Nanoscale kinetic segregation of TCR and CD45 in engaged microvilli facilitates early T cell activation. *Nat. Commun.* **9**, 732.
- Rollins, G.C., Shin, J.Y., Bustamante, C., and Pressé, S. (2015). Stochastic approach to the molecular counting problem in superresolution microscopy. *Proc. Natl. Acad. Sci. USA* **112**, E110–E118.
- Roob, E., 3rd, Trendel, N., Rein Ten Wolde, P., and Mugler, A. (2016). Cooperative Clustering Digitizes Biochemical Signaling and Enhances its Fidelity. *Biophys. J.* **110**, 1661–1669.
- Rossboth, B., Arnold, A.M., Ta, H., Platzer, R., Kellner, F., Huppa, J.B., Bramehuber, M., Baumgart, F., and Schütz, G.J. (2018). TCRs are randomly distributed on the plasma membrane of resting antigen-experienced T cells. *Nat. Immunol.* **19**, 821–827.
- Rossey, J., Owen, D.M., Williamson, D.J., Yang, Z., and Gaus, K. (2013). Conformational states of the kinase Lck regulate clustering in early T cell signaling. *Nat. Immunol.* **14**, 82–89.
- Rossey, J., Cohen, E., Gaus, K., and Owen, D.M. (2014). Method for co-cluster analysis in multichannel single-molecule localisation data. *Histochem. Cell Biol.* **141**, 605–612.
- Rubin-Delanchy, P., Burn, G.L., Griffié, J., Williamson, D.J., Heard, N.A., Cope, A.P., and Owen, D.M. (2015). Bayesian cluster identification in single-molecule localization microscopy data. *Nat. Methods* **12**, 1072–1076.
- Rust, M.J., Bates, M., and Zhuang, X. (2006). Sub-diffraction-limit imaging by stochastic optical reconstruction microscopy (STORM). *Nat. Methods* **3**, 793–795.
- Santos, A.M., Ponjavic, A., Fritzsche, M., Fernandes, R.A., de la Serna, J.B., Wilcock, M.J., Schneider, F., Urbančić, I., McColl, J., Anzilotti, C., et al. (2018). Capturing resting T cells: the perils of PLL. *Nat. Immunol.* **19**, 203–205.
- Schmedt, C., Saijo, K., Niidome, T., Kühn, R., Aizawa, S., and Tarakhovskiy, A. (1998). Csk controls antigen receptor-mediated development and selection of T-lineage cells. *Nature* **394**, 901–904.
- Schnitzbauer, J., Strauss, M.T., Schlichthaerle, T., Schueder, F., and Jungmann, R. (2017). Super-resolution microscopy with DNA-PAINT. *Nat. Protoc.* **12**, 1198–1228.
- Sherman, E., Barr, V., and Samelson, L.E. (2013). Super-resolution characterization of TCR-dependent signaling clusters. *Immunol. Rev.* **251**, 21–35.
- Siminovitch, K.A. (2004). PTPN22 and autoimmune disease. *Nat. Genet.* **36**, 1248–1249.
- Stanford, S.M., and Bottini, N. (2014). PTPN22: the archetypal non-HLA autoimmunity gene. *Nat. Rev. Rheumatol.* **10**, 602–611.
- Suzuki, K.G.N., Fujiwara, T.K., Edidin, M., and Kusumi, A. (2007). Dynamic recruitment of phospholipase C γ at transiently immobilized GPI-anchored receptor clusters induces IP3-Ca²⁺ signaling: single-molecule tracking study 2. *J. Cell Biol.* **177**, 731–742.
- Thomas, S., Xue, S.A., Bangham, C.R.M., Jakobsen, B.K., Morris, E.C., and Stauss, H.J. (2011). Human T cells expressing affinity-matured TCR display accelerated responses but fail to recognize low density of MHC-peptide antigen. *Blood* **118**, 319–329.
- Torgersen, K.M., Vang, T., Abrahamsen, H., Yaqub, S., Horejší, V., Schraven, B., Rolstad, B., Mustelin, T., and Taskén, K. (2001). Release from tonic inhibition of T cell activation through transient displacement of C-terminal Src kinase (Csk) from lipid rafts. *J. Biol. Chem.* **276**, 29313–29318.
- van Zanten, T.S., Cambi, A., Koopman, M., Joosten, B., Figdor, C.G., and Garcia-Parajo, M.F. (2009). Hotspots of GPI-anchored proteins and integrin nanoclusters function as nucleation sites for cell adhesion. *Proc. Natl. Acad. Sci. USA* **106**, 18557–18562.
- Vang, T., Congia, M., Macis, M.D., Musumeci, L., Orrú, V., Zavattari, P., Nika, K., Tautz, L., Taskén, K., Cucca, F., et al. (2005). Autoimmune-associated lymphoid tyrosine phosphatase is a gain-of-function variant. *Nat. Genet.* **37**, 1317–1319.
- Vang, T., Liu, W.H., Delacroix, L., Wu, S., Vasile, S., Dahl, R., Yang, L., Musumeci, L., Francis, D., Landskron, J., et al. (2012). LYP inhibits T-cell activation when dissociated from CSK. *Nat. Chem. Biol.* **8**, 437–446.
- Vang, T., Nielsen, J., and Burn, G.L. (2018). A switch-variant model integrates the functions of an autoimmune variant of the phosphatase PTPN22. *Sci. Signal.* **11**, 526.
- Veillette, A., Rhee, I., Souza, C.M., and Davidson, D. (2009). PEST family phosphatases in immunity, autoimmunity, and autoinflammatory disorders. *Immunol. Rev.* **228**, 312–324.
- Voisinne, G., Kersse, K., Chaoui, K., Lu, L., Chaix, J., Zhang, L., Goncalves Meinoita, M., Girard, L., Ounoughene, Y., Wang, H., et al. (2019). Quantitative interactions in primary T cells unveils TCR signal diversification extent and dynamics. *Nat. Immunol.* **20**, 1530–1541.
- Wallis, A.M., Wallace, E.C., Hostager, B.S., Yi, Z., Houtman, J.C.D., and Bishop, G.A. (2017). TRAF3 enhances TCR signaling by regulating the inhibitors Csk and PTPN22. *Sci. Rep.* **7**, 2081.
- Williamson, D.J., Owen, D.M., Rossey, J., Magenau, A., Wehrmann, M., Gooding, J.J., and Gaus, K. (2011). Pre-existing clusters of the adaptor Lat do not participate in early T cell signaling events. *Nat. Immunol.* **12**, 655–662.
- Williamson, D.J., Burn, G.L., Simoncelli, S., Griffié, J., Peters, R., Davis, D.M., and Owen, D.M. (2020). Machine learning for cluster analysis of localization microscopy data. *Nat. Commun.* **11**, 1493.
- Xu, S., Huo, J., Tan, J.E.-L., and Lam, K.-P. (2005). Cbp deficiency alters Csk localization in lipid rafts but does not affect T-cell development. *Mol. Cell Biol.* **25**, 8486–8495.
- Zhang, J., Zahir, N., Jiang, Q., Miliotis, H., Heyraud, S., Meng, X., Dong, B., Xie, G., Qiu, F., Hao, Z., et al. (2011). The autoimmune disease-associated PTPN22 variant promotes calpain-mediated Lyp/Pep degradation associated with lymphocyte and dendritic cell hyperresponsiveness. *Nat. Genet.* **43**, 902–907.
- Zikherman, J., Hermiston, M., Steiner, D., Hasegawa, K., Chan, A., and Weiss, A. (2009). PTPN22 deficiency cooperates with the CD45 E613R allele to break tolerance on a non-autoimmune background. *J. Immunol.* **182**, 4093–4106.

STAR★METHODS

KEY RESOURCES TABLE

REAGENT or RESOURCE	SOURCE	IDENTIFIER
Antibodies		
CD3 Monoclonal Antibody (OKT3), Functional Grade, eBioscience	Thermo Fisher Scientific	Cat# 16-0037-85; RRID: AB_468855
CD28 Monoclonal Antibody (CD28.2), Functional Grade, eBioscience	Thermo Fisher Scientific	Cat# 16-0289-85; RRID: AB_468927
Rabbit monoclonal against PTPN22 (D6D1H)	Cell Signaling Technology	Cat# 14693; RRID: AB_2798575
Rabbit polyclonal against Phospho-Lck (Tyr505)	Cell Signaling Technology	Cat# 2751; RRID: AB_330446
Purified Mouse monoclonal Anti- ZAP-70 Kinase Clone 29/ZAP70 Kinase	BD Biosciences	Cat#: 610239; RRID:AB_397634
Mouse monoclonal antibodies against Csk (E-3)	Santa Cruz, Biotechnology	Cat# sc-166560; RRID: AB_2084154
Mouse monoclonal antibodies against Cbp/PAG (G-8)	Santa Cruz, Biotechnology	Cat# sc-365387; RRID:AB_10846188
Mouse monoclonal antibodies against TRAF3 (G-6)	Santa Cruz, Biotechnology	Cat# sc-6933; RRID:AB_628390
Goat anti-rabbit pAb (HRP conjugated)	Agilent Dako	P044801-2; RRID: AB_2617138
Rabbit anti-mouse pAb (HRP conjugated)	Agilent Dako	P026002-2; RRID: AB_2636929
anti-ERK1/2 Phospho (Thr202/Tyr204) Antibody	Biologend	Cat# 369505; RRID:AB_2629704
Mouse anti-Lck mAb (Clone 3A5)	Thermo Fisher Scientific	Cat#: MA5-12303; RRID:AB_10986446
GAPDH XP Rabbit mAb (HRP conjugated)	Cell Signaling Technology	Cat#: 8884S; RRID:AB_11129865
Phospho-Zap-70 (Tyr319)/Syk (Tyr352) (65E4)	Cell Signaling Technology	Cat#: 2717S; RRID:AB_2218658
Goat anti-Rabbit IgG (H+L), Superclonal Recombinant Secondary Antibody, Alexa Fluor 647	Thermo Fisher Scientific	Cat#: A27040; RRID:AB_2536101
Chemicals, Peptides, and Recombinant Proteins		
RPM1 1640 Medium	Thermo Fisher Scientific	Cat#: 21875091
L-Glutamine (200 mM)	Thermo Fisher Scientific	Cat#: 25030024
Heat inactivated Fetal Bovine Serum	GIBCO	Cat#: 16140-071
GIBCO DPBS, no calcium, no magnesium	Thermo Fisher Scientific	Cat#: 14190169
16% (vol/vol) Paraformaldehyde	Electron Microscopy Sciences	Cat#:15710
25% (vol/vol) Glutaraldehyde	Sigma Aldrich	Cat#: G5882
Hank's balanced salt solution (HBBS) No phenol red	Thermo Fisher Scientific	Cat#: 14025100
Protease Inhibitor Cocktail (100X)	Cell Signaling Technology	Cat#: 5871
RIPA buffer (10X)	Cell Signaling Technology	Cat#: 9806
4x Laemmli Sample Buffer	Bio-Rad	Cat#: 1610747
2-mercaptoethanol	Sigma Aldrich	Cat#: M6250
poly-L-lysine (0.1%)	Santa Cruz, Biotechnology	Cat#: sc-286689
Bovine Serum Albumin	Sigma-Aldrich	Cat#: A4503
Sodium Chloride	VWR	Cat#:443827W
Ammonium Chloride	Sigma Aldrich	Cat#: A9434
PIPES dipotassium salt	Sigma Aldrich	Cat#: P7643
Magnesium chloride (1M)	Ambion	Cat#: AM9530G
EGTA	VWR	Cat#: 437013D
EDTA (0.5M)	Thermo Fisher Scientific	Cat#:15575-020
Lysolecithin (L- α -Lysophosphatidylcholine)	Sigma Aldrich	Cat#: L4129
Gold nanoparticles 100nm	BBI solutions	SKU #: EM.GC100
FOXP3 Perm Buffer 10x	Biologend	Cat#: 421402
Maleimide-PEG2-succinimidyl ester	Sigma-Aldrich	Cat#: 746223
No-Weigh Format DTT	Thermo Fisher Scientific	Cat#: 20291

(Continued on next page)

Continued

REAGENT or RESOURCE	SOURCE	IDENTIFIER
2D DNA-origamis (commercial custom-made)	GATTAquant GmbH	N/A
Pierce Bovine Serum Albumin, Biotinylated	Thermo Fisher Scientific	Cat#: 29130
Streptavidin	Thermo Fisher Scientific	Cat#: S888
TE, pH 8.0, RNase-free	Thermo Fisher Scientific	Cat#: AM9849
Tween 20	Thermo Fisher Scientific	Cat#: BP337-500
Critical Commercial Assays		
SuperSignal West Pico PLUS Chemiluminescent Substrate	Thermo Fisher Scientific	Cat#: 34077
Experimental Models: Cell Lines		
Jurkat TCR ^{-/-} pTax ^{+/+} PTPN22 ^{-/-} cells	Bray et al., 2018	https://doi.org/10.3389/fimmu.2018.02595
Jurkat TCR ^{-/-} pTax ^{+/+} PTPN22 ^{+/+} cells	Bray et al., 2018	https://doi.org/10.3389/fimmu.2018.02595
Oligonucleotides		
Docking Strand Csk Antibody: 5'-ATCTAAGTATT-Thiol	biomers.net GmbH	N/A
Docking Strand PAG Antibody: 5'-TAGGTAATATT-Thiol	biomers.net GmbH	N/A
Docking Strand TRAF3 Antibody: 5'-TATGTAACITTT-Thiol	biomers.net GmbH	N/A
Imager Strand for Csk: ATTO655-TACTTAGATG-3'	biomers.net GmbH	N/A
Imager Strand for PAG: ATTO655-TATTACCTAG-3'	biomers.net GmbH	N/A
Imager Strand for TRAF3: ATTO655-AGTTACATAC-3'	biomers.net GmbH	N/A
Software and Algorithms		
ImageJ	NIH	https://imagej.nih.gov/ij/
Picasso	Schnitzbauer et al., 2017	https://github.com/jungmannlab/picasso
Bayesian-based cluster analysis (original)	(Griffié et al., 2016)	https://www.nature.com/articles/nprot.2016.149
MATLAB R2018b	MathWorks	https://uk.mathworks.com/products/matlab.html
GraphPad Prism 6.0	GraphPad	https://www.graphpad.com/
R v3.1.2	The R Foundation	https://cran.r-project.org/
RStudio v1.0.136	RStudio	https://rstudio.com/
FlowJo V.10.1 software	Tree Star Inc.	https://www.flowjo.com
Custom-written MATLAB Code and Bayesian-based cluster analysis implemented for 3 color dataset	This paper	https://github.com/Owenlab-UoB
Other		
Illustra MicroSpin G-25 column	GE Healthcare	SKU#: GE27-5325-01
Zeba Spin Desalting Columns, 7K MWCO, 0.5 mL	Thermo Fisher Scientific	Cat#: 89882
Amicon spin filters, 100 kDa	Merck/EMD Millipore	Cat.#: UFC510096
ibidi μ -Slide VI 0.5 chamber	ibidi GmbH	Cat.#: 80607

RESOURCE AVAILABILITY

Lead Contact

Further information and requests for resources and reagents should be directed to and will be fulfilled by the Lead Contact Dylan M. Owen (d.owen@bham.ac.uk).

Materials Availability

This study did not generate new unique reagents.

Data and Code Availability

All experimental data produced for this manuscript are available from the Lead Contact (d.owen@bham.ac.uk) upon reasonable request. All the code for data analysis is available at <https://github.com/Owenlab-UoB>.

EXPERIMENTAL MODELS AND SUBJECT DETAILS

TCR^{-/-} Jurkat cells were obtained from Hans Stauss, University College London and maintained in Roswell Park Memorial Institute (RPMI-1640, GIBCO) medium supplemented with 10% fetal bovine serum (FBS, GIBCO) and 5 mM L-glutamine and cultured at 37°C, 5% CO₂ in a humidified incubator. Retroviral transduction of TCR constructs was performed as described (Thomas et al., 2011) and one clone with high expression for a pTax peptide (LLFGYPVYV, derived human T-lymphotropic virus type 1) was selected as the parent line for the Crispr/Cas mediated PTPN22 deletion. PTPN22 KO Jurkat clone was produced by transfecting the selected parent line with plasmids containing Cas9, sgRNA sequences targeting PTPN22 Exon 1, and a GFP reporter as described in Bray et al. (2018). Western blot and PTPN22 Exon 1 region sequencing confirmed the deletion of PTPN22 protein in the KO cell line. The PTPN22 wild-type (WT) cell line was obtained by transfecting the same parent cell line using only the GFP reporter construct.

METHOD DETAILS

Antibodies and DNA

Rabbit monoclonal and polyclonal antibodies against PTPN22 (D6D1H), pLck (Tyr505), pZap-70 (Try319) and GAPDH were from Cell Signaling Technology. Mouse monoclonal antibody against ZAP-70 (29/ZAP70 Kinase) was from BD Biosciences. Mouse monoclonal antibodies against Lck (Clone 3A5), CD3 (OKT3), CD28 (CD28.2), and secondary anti-rabbit Alexa Fluor 647 were from Thermo Fisher Scientific. Mouse monoclonal antibody against pERK1/2 (Thr202/Tyr204) clone 6B8B69 was from Biolegend. Mouse monoclonal antibodies against Csk (E-3); Cbp/PAG (G-8); TRAF3 (G-6) were from Santa Cruz, Biotechnology and its conjugation to DNA-PAINT docking strands was performed using maleimidePEG2-succinimidyl ester coupling reaction according to a published protocol (Schnitzbauer et al., 2017) as described below. Secondary anti-rabbit and anti-mouse-HRP antibodies were from Dako. All DNA reagents were from biomers.net GmbH. DNA docking strands sequences for Csk, PAG and TRAF3 target proteins were 5'-ATCT AAGTATT-Thiol, 5'-TAGGTAATATT-Thiol and 5'-TATGTAAC TTT-Thiol, respectively. While the corresponding DNA imager strand sequences used were ATTO655-TACTTAGATG-3', ATTO655-TATTACCTAG-3' and ATTO655-AGTTACATAC-3'.

DNA-antibody coupling reaction

DNA labeling of a monoclonal primary antibodies was performed using the maleimidePEG2-succinimidyl ester coupling reaction (Jungmann et al., 2014). To reduce the thiolated DNA for the maleimide reaction, 13 μL of the corresponding 1 mM thiol-DNA was incubated with 30 μL of a freshly prepared 250 mM DDT (Thermo Fisher Scientific) solution (1.5 mM EDTA, 0.5x PBS, pH 7.2) on a shaker, in the dark, for 2 h at room temperature. 30 min after the reduction of the thiol-DNA started, 50 μL of 13 μM antibody was incubated with 0.5 μL of 23.5 mM Maleimide-PEG2-succinimidyl ester (Sigma-Aldrich) solution on a shaker, in the dark, for 90 min at 4°C. Prior DNA-antibody conjugation, both sets of reactions were purified using an Illustra MicroSpin G-25 column (GE Healthcare) to remove excess of DDT and a Zeba desalting column (Thermo Fisher Scientific) to remove excess of cross-linker. Next, both flow-through of the columns were mixed and incubated on a shaker, in the dark, overnight at 4°C. The next day, DNA excess was removed by Amicon spin filtration (100 kDa). Antibody-DNA concentration was measured with the NanoDrop 2000 spectrophotometer (Thermo Scientific) and adjusted to 2.5 μM with PBS. Likewise, spectrophotometric analysis was performed to quantify the DNA-antibody coupling ratio and found to be ~1.3 in average for all the oligo-coupled primary antibodies.

Western blotting

WT and PTPN22 KO T cells were harvested, washed in PBS and lysed in RIPA buffer (Cell Signaling Technology) with protease inhibitor cocktail (Biolegend). Lysates were added to Laemmli sample buffer (Bio-Rad) with 10% 2-mercaptoethanol, resolved on SDS-PAGE gels and transferred to Immobilon-P polyvinylidene difluoride membranes and blocked with 5% BSA in TBST. After incubation with the corresponding primary and secondary antibodies diluted in 5% BSA in TBST, proteins were visualized by SuperSignal chemiluminescent reaction (Pierce Biotechnology) in a ChemiDoc station (Bio-Rad).

Phospho flow cytometry

1.5 million WT and PTPN22 KO T cells per condition were added to a 24-well plate, coated with plate-bound PLL or anti-CD3 (2 μg/ml) plus anti-CD28 (5 μg/ml). Plates were briefly spun (3 s at 300xg) to ensure cells were on the plate bottom, and then placed in the incubator for the indicated time. Cells were fixed with 3% paraformaldehyde, washed, and stained with APC conjugated anti-ERK1/2 pThr202/Thy204, or anti-Lck pTry505 or anti-Zap-70 pTry319 overnight at 4°C in FOXP3 perm buffer (Biolegend). T cells were analyzed with a BD LSRFortessa or FACSCanto II (BD Biosciences), and analysis conducted using FlowJo V.10.1 software (Tree Star Inc.).

Immunofluorescence staining

Six-channel glass-bottomed microscopy chambers (μ-Slide VI 0.5, Ibidi) were coated overnight at 4°C with 50 μL of anti-CD3 (8 μg/ml, clone OKT3) and anti-CD28 (20 μg/ml, clone CD28.2) or for 10 min at room temperature with 0.01% poly-L-lysine (PLL), washed three times in PBS and left in Hank's balanced salt solution (HBBS) before use. T cells were resuspended at 3x10⁶ cells/mL in HBBS and immediately added to the coated glass chambers. Following 2 or 8 min of incubation at 37°C, the cells were pH

shift-fixed for 90 min with a 4% paraformaldehyde (PFA) and 0.2% glutaraldehyde solution in PEM buffer (80 mM Pipes dipotassium salt, supplemented with 2 mM $MgCl_2$ and 5 mM EGTA, pH 6.8) at 25°C. Following permeabilization for 10 min at 25°C with 0.01% lysolecithin, samples were treated with 20 mM NH_4Cl for 10 min at room temperature to quench autofluorescence. The chambers were then block with 5% bovine serum albumin (BSA) for 2 hours and incubated with 0.1 μM DNA-conjugated primary antibodies in 5% BSA in PBS at 4°C overnight. Cells were fixed again with a 2% PFA solution in PBS for 5 min at 25°C, followed by 3x washes with PBS. 100 nm gold nanoparticles (BBI solutions) were added as fiducial markers for drift correction by incubating the sample for 5 min in a 1:2 solution of nanoparticles in PBS and washed 3 x washes with PBS, and 3 x with PAINT buffer (1x PBS supplemented with 500 mM NaCl). Samples were then used immediately for DNA-PAINT imaging.

T cell imaging conditions

Exchange DNA-PAINT imaging was performed on a Nikon N-STORM microscope equipped with a 100 × 1.49 numerical aperture oil immersion TIRF objective and a Perfect Focus System. Samples were imaged under TIRF illumination with a 647 nm laser line (~2 kW/cm²) that was coupled into the microscope objective using a quad band set for TIRF (Chroma 89902-ET-405/488/561/647 nm). Fluorescence light was imaged on an EMCCD camera (iXon DU-897U, Andor Technologies) with a final pixel size of 160 nm in the focal plane. For fluid exchange we connected the ibidi μ -Slide VI 0.5 chamber with a silicon tubing (Silicon Tubing 0.5 mm ID, Ibidi) via a suitable adaptor (Elbow Luer Connector Male, Ibidi). Each imaging acquisition step was performed by adding the corresponding 5 nM Atto 655-labeled DNA imager strand in PAINT buffer to the sample (biomers.net GmbH) followed by a 5 min washing step (corresponding to 10 mL of PAINT buffer). Before the next imager strand solution was introduced, we monitored the camera readout to ensure complete exchange of imager solutions. Sequential imaging and washing steps were performed until all three target proteins (Csk, PAG and TRAF3) were imaged. We acquired, for each imaging step, sequences of 10,000 frames at 10 Hz acquisition rate with an electron multiplier gain of 50 and pre-amp gain profile 1.

Reconstruction of proteins maps and data analysis

x,y localizations coordinates from the raw fluorescent DNA-PAINT imaging experiments were obtained using the 'Localize' module of Picasso software (Schnitzbauer et al., 2017). Localizations with uncertainties greater than 15 nm were removed while no merging was performed for molecules re-appearing in subsequent frames. Drift correction and multi-color data alignment was performed using a combination of redundant cross-correlation and fiducial markers approach with the 'Render' module of Picasso. Super-resolution image rendering was done by plotting each localization as a Gaussian probably function with standard deviation equal to its localization precision.

To convert the list of x,y localizations into a list of x,y molecular coordinates we further processed the data using a combination of Bayesian-based cluster analysis algorithms, k -means clustering and the prior knowledge of the expected number of single-molecule localizations per docking strand (see Figure S2). First, we randomly selected thirty non-overlapping 2 μm × 2 μm regions of interest (ROIs) for the analysis of each time-course point experiment (before and following 2- and 8-min TCR stimulation), with a maximum of three ROIs per cell. To avoid suboptimal clustering results; ROIs were selected such that they do not intersect with cell boundaries. To identify sets of localizations arising from a real docking strand target, we analyzed the data using a robust cluster analysis technique based on Ripley's K function, Bayesian statistics and topographical prominence (Griffié et al., 2016, 2017; Rubin-Delanchy et al., 2015). Analysis parameters (prior settings) were choose as default (see Table S5) as they genuinely represented the experimental localization-based datasets: (i) cluster-analysis in micron-sized regions; (ii) 20 - 80% of the localizations are in clusters; (iii) radius of the cluster into the 10-500 nm region. Non-cluster points and points attributed to a cluster with fewer than 26 localizations were discarded because they are likely to correspond to noise. This cut-off value was chosen as it is the largest value that gives a cumulative probability of 1 of getting cluster of points with more than that number of localizations (i.e., $P(n \geq 26) = 1$, where n is the number of localizations). For this consideration we assumed that single molecule localizations are distributed as a Poisson process and we experimentally calibrated that a single docking strand yields, on average, ~52 localizations per 10k frames (see Figure S2). To recover the most accurate descriptors (x,y molecular coordinates) for the distribution of proteins underlying the detected distribution of clustered localizations, we implemented a k -means clustering strategy in MATLAB (see Figure S2E). The k -means algorithm simply partitions a number of observations (i.e., x,y localization coordinates per cluster) into k sets; returning as a result each set center (i.e., x,y molecular coordinates). The value k , calculated for each detected cluster of localizations, was estimated to be the ratio between the number of localizations within a cluster and the expected number of localizations per docking strand (see Figure S2C).

To quantify the level and size scale of proteins clustering, we further analyzed the generated x,y molecular coordinates using the topographical prominence Ripley's K based Bayesian model (Griffié et al., 2018). Cluster points of proteins (i.e., x,y molecular coordinates) are much less dense than cluster points of single-molecule localizations (i.e., x,y localization coordinates). Therefore, to detect these small protein clusters, which are defined as an assemblage containing at least four proteins, we choose priors that increase the typical detectability limit of around six points per cluster. Particularly, we decreased the prior of the percentage of non-clusters points from the default value of 50% to 20%. We also chose as a prior a wider cluster size distribution weighted toward smaller radius values with respect to the ones used for the single-molecule localizations dataset (Table S5). This last step was necessary because k -means clustering partitions the data so as to minimize the distances within the sets, and as such, protein cluster sizes will be underestimated.

Mixed protein cluster analysis

To assess the existence of mixed protein clusters, we merged the stack of generated pseudo-color molecular localizations coordinates (Csk, PAG and TRAF3) into a single x, y coordinate list keeping the identity of the pseudo-color for each point (merged dataset). Bayesian-based cluster analysis was performed on the merged dataset similar to the one-color dataset as described above; using priors that are bias toward the detection of small mixed protein clusters (Table S5). Output data provided both, a label that assigned whether a point was or not in a clustered, with the identity of that cluster, and an extra label identifying the corresponding pseudo-color of each point in the cluster. This information permitted allocating to each detected cluster its corresponding protein percentage composition. Mixed protein clusters were considered as such, only when, there were at least two molecular units of each cluster combination type in the cluster. Otherwise, the cluster was assigned as pure in the component with higher percentage. To ease graphical representation, each detected mixed protein cluster was depicted as a point in a ternary plot. Every point in the ternary plot represents a different composition of a three-component system, such that the 100% of components R (Csk), G (TRAF3) and B (PAG) are located in each of the vertices of an equilateral triangle. Therefore, the coordinates (in the cartesian plane) of a sample comprising 100% R (Csk) will be located at the top of the triangle, $(x, y) = (1/2; \sqrt{3}/2)$, 100% B (PAG) at the lower right corner of the triangle, $(x, y) = (1, 0)$ and 100% G (TRAF3) at the lower left corner, $(x, y) = (0, 0)$. An arbitrary mixture of three species (R, G, B) will be located at $(x, y) = (1/2 * (2B+R)/(R+G+B), \sqrt{3}/2 * R/(R+G+B))$ on the plane (within the triangle) (see Figure S4A). To simplify graph readout, we have also assigned the color Red, Green and Blue to pure clusters of Csk, TRAF3 and PAG, respectively, with mixed clusters having the corresponding RGB color combination given by the % of each component in the cluster. Furthermore, we depicted a circle for each of the main cluster combinations (Csk-PAG, Csk-TRAF3, PAG-TRAF3 and Csk-PAG-TRAF3) with its position being the most likely cluster composition for that combination, and with the size representing the contribution of that cluster combination type with respect to all the found mixed clusters. To evaluate the significance of the detected merged clusters, we compared them with an artificial merged dataset obtained by randomly mixing the same experimental individual single-color protein maps and analyzed them using the same pipeline as described above.

Calibration of DNA-PAINT imaging

The reversible binding kinetic between docking and imaging strands in DNA-PAINT data allows to estimate the fraction of time (binding probability) that a number of DNA-docking strands (binding sites), N_{BS} , will be bound during the acquisition time of the experiment. Such that, when averaged over a long enough time, the binding probability, will be given by $N_{localizations}/N_{frames}$.

There are different approaches to derive an equation that relates the number of binding sites with the number of localizations per frame. One possible derivation, expanded in this section, is to use ligand-receptor binding kinetics. We consider first a single docking site, that can transiently bind to the imager with association and dissociation rate constants given by an k_{ON} and k_{OFF} , respectively. Then, in equilibrium, the fraction of docking sites having an imager bound is given by f_B . Note that since each site is independent from the other, f_B is also equal to the probably that a single docking site has one imager bound, $p_{bind,1BS}$. Thus, following the ligand-receptor binding kinetics model,

$$p_{bind,1BS} = \frac{[I]}{[I] + k_{OFF}/k_{ON}} = \frac{1}{1 + \tau_{dark}/\tau_{bright}} \quad (\text{eq. 1})$$

where $[I]$ is the concentration of imager strand in solution; τ_{bright} is equal to $1/k_{OFF}$ and is in the order of 0.5 – 0.6 s for 9 base-pair double stranded DNA binding; and τ_{dark} is equal to $1/k_{ON}[I]$ with k_{ON} being in the order of $2.3 - 1.6 \cdot 10^6 \text{ M}^{-1} \text{ s}^{-1}$ (Jungmann et al., 2010).

Then, if $\tau_{dark}/\tau_{bright} \gg 1$ (as for the case when the probability of having more than one site simultaneously occupied is negligible), then the probability of N_{BS} binding sites being occupied, $p_{bind,N_{BS}}$, is simply obtained by multiplying $p_{bind,1BS}$ with the number of binding sites,

$$p_{bind,N_{BS}} \approx N_{BS} p_{bind,1BS} \approx \frac{N_{localizations}}{N_{frames}} \approx \frac{N_{BS}}{\tau_{dark}/\tau_{bright}} \quad (\text{eq. 2})$$

Knowing the experimental concentration of imager strand used and the total number of detected frames; we can estimate the number of localizations that we expect, on average, for a given number of DNA-docking strands (Figure S2C, blue dashed line). Likewise, we can use this linear approximation to predict that for our experimental conditions - i.e., a concentration of imager strand of 5 nM and an image stack of 10,000 frames - each docking strand will be detected as a cluster of ca. 40 – 68 localizations depending on exact binding kinetic parameters

To determine the sensitivity and the dynamic range of the linear approximation, we experimentally imaged (Figure S2E) or stochastically simulated (Figure S2B) single-molecule localization data of DNA origami nanostructures. DNA origami nanostructures offer the possibility to fabricate trillions of identical objects at once while achieving high-specificity and precise positioning of single capturing probes in the nanoscale. As such, they can be used as a breadboard to carry a pre-defined number of DNA-docking strands on their surface (Figure S2B). Experimentally, visual inspection of each DNA origami defines the number of true docking strands incorporated in the structure (binding sites), which can be different for each individual rectangular shape origami. For simulated data, we can input to have 100% incorporation of the docking strands in each of the different type of simulated DNA-origami breadboards (see 2D DNA-origami simulations below). By comparing the number of docking strands (binding sites) with the number of detected single-molecule localization, we

can directly determine how many single-molecule localizations we expect to see per each docking strand. Experimentally, we found that number to be 52 localizations per 10k frames, which correlates with having an association (k_{ON}) rate of $1.7 \text{ M}^{-1} \text{ s}^{-1}$ and τ_{bright} of 0.6 s.

2D DNA-origami simulations and analysis

For the simulations of Figure S2, we used the ‘Simulate’ module of Picasso software (Schnitzbauer et al., 2017). Simulations were performed using 1, 4, 9, 16, 25, 36 (for Figures S2B and S2C) or 9 (for Figures S2I–S2N) docking sites on rectangular shape DNA-origami as model input assuming 100% incorporation of the docking strands. Association (k_{ON}) and dissociation (k_{OFF}) rates were chosen to be $1.7 \cdot 10^6 \text{ M}^{-1} \text{ s}^{-1}$ and 1.7 s^{-1} , respectively, as they match with the average number of localizations observed in the our DNA-origami experimental data and they are also in keeping with the typical binding kinetics between 9 base-pair single-stranded DNAs (Jungmann et al., 2010). Imager strand concentration, frame rate and total number of frames were set equal to the experimental conditions: 5 nM, 10 Hz and 10,000 frames, respectively. Simulated data was analyzed using the ‘Localize’ and ‘Render’ module of Picasso, which allows quantifying the detected number of localizations per simulated origami. 100 (Figures S2B and S2C) or 50 (Figures S2I–S2N) origamis of each type were simulated, and the mean number of localizations was plotted with its corresponding standard deviation as depicted in Figure S2C.

2D DNA-origami calibration sample and analysis

2D commercial custom made DNA-origami sheets of $\sim 70 \times 90 \text{ nm}$ dimensions (GATTAquant GmbH, Braunschweig, Germany) carrying nine docking (5'-ATTACTTCTTT-3') strands, separated ca. 26 nm from each other, were used to verify the theory and experimentally calibrate the expected number of localizations per molecular target. Biotinylated DNA origami sheets were immobilized on BSA-biotin-neutravidin coated glass-bottomed 6-channel slides (#1.5 glass, μ -Slide VI 0.4, Ibbidi) according to the vendor's protocol. Briefly, two buffers were used for the DNA-origami samples immobilization: Buffer A+ comprised of 10 mM Tris-HCl, 100 mM NaCl and 0.05% Tween 20 at pH 8.0 and Buffer B+ which consists of 5 mM Tris-HCl, 10 mM MgCl_2 , 1 mM EDTA and 0.05% Tween 20 at pH 8.0. To coat the surface of the glass slides, first, 80 μl of BSA-biotin solution (1mg/ml in Buffer A+, Sigma-Aldrich) was added to the channel and incubated it for 5 min. After washing the channel with 180 μl of Buffer A+, 40 μl of streptavidin solution (1mg/ml in Buffer A+, Thermo Fisher Scientific) was incubated twice for 5 min. The channel was then washed with 180 μl of Buffer A+ and 180 μl of Buffer B+ prior DNA incubation. DNA-origami stock sample was diluted 1:10 in Buffer B+ and added to the channel for 20 min, followed by 2x washes with 100 μl of Buffer B+. Following DNA-origami immobilization, 100 nm gold nanoparticles fiducial markers (BBI solutions) were added and incubated for 5 min (diluted 1:2 in PBS + 5 mM MgCl_2). Gold nanoparticles excess was rinsed 3 \times with Buffer B+. For TIRF-SMLM imaging, 5 nM fluorescently labeled DNA imager strand (ATTO655-TACTTAGATG-3') was added to the PAINT buffer (1x PBS supplemented with 500 mM NaCl) and loaded into the channel. Samples were then used immediately for DNA-PAINT imaging, using the same experimental setup and conditions described previously.

x, y localizations coordinates and super-resolution images were obtained and reconstructed from the raw fluorescent imaging data. We used the pick tool of the ‘Render’ module of Picasso to quantify the number of detected localizations per origami and compared it to the number of observable docking sites as showed in Figure S2C.

QUANTIFICATION AND STATISTICAL ANALYSIS

DNA-PAINT, western blotting and phospho flow cytometry data correspond to three independent experiments. For DNA-PAINT imaging a total of thirty $4 \mu\text{m}^2$ regions, obtained from 10–15 WT and PTPN22-KO T cells were analyzed per condition (PLL, 2- or 8-min stimulation). Statistical analyses were performed using Prism 6.0 software (GraphPad). The distributions of data points and their variance were determined, and parametric or non-parametric test were utilized as appropriate. Comparison between two groups were evaluated using an unpaired, two-tailed, Mann-Whitney U test or Student's t test for normally distributed data. Groups of three or more were compared using the rank-based nonparametric Kruskal-Wallis H test or Tukey's ordinary one-way ANOVA multiple comparison test for normally distributed data. Differences were considered to be statistically significantly different when $p < 0.05$ for rejecting the null hypothesis.